Rapid and efficient room temperature serial synchrotron crystallography

Kara Zielinski[1,*,$], Andreas Prester[2,*], Hina Andaleeb[3,*,$$], Soi Bui[4], Oleksandr Yefanov[1], Lucrezia Catapano[4], Alessandra Henkel[1], Max Wiedorn[1], Olga Lorbeer[5], Eva Crosas[5], Jan Meyer[5], Valerio Mariani[1,$$$], Martin Domaracky[1], Thomas A. White[5], Holger Fleckenstein[1], Iosifina Sarrou[1,$$$$], Nadine Werner[3], Gleb Bourenkov[6], Christian Betzel[3,7], Holger Rohde[2], Martin Aepfelbacher[2], Henry N. Chapman[1,7,8], Markus Perbandt[3], Roberto A Steiner[4,5#], Dominik Oberthür[1,#]

Affiliations:

1 CFEL, Center for Free-Electron Laser Science, Deutsches Elektronen-Synchrotron DESY, Notkestraße 85, 22607 Hamburg, Germany

2 Institute for Medical Microbiology, Virology and Hygiene, University Medical Center Hamburg-Eppendorf, Martinistrasse 52, 20246, Hamburg, Germany

3 Institute of Biochemistry and Molecular Biology, Laboratory for Structural Biology of Infection and Inflammation, University of Hamburg, c/o DESY, Build. 22a. Notkestr. 85, 22603 Hamburg, Germany

4 Randall Centre of Cell and Molecular Biophysics, King's College London, UK.

5 Deutsches Elektronen-Synchrotron DESY, Notkestraße 85, 22607 Hamburg, Germany

6 EMBL Outstation Hamburg, c/o DESY, Notkestr. 85, 22607 Hamburg, Germany.

7 Hamburg Centre for Ultrafast Imaging, Universität Hamburg, Luruper Chaussee 149, 22761 Hamburg, Germany.

8 Department of Physics, University of Hamburg, Luruper Chaussee 149, 22761 Hamburg, Germany.

9 Dept of Biomedical Sciences, University of Padova, Italy

Current Affiliation:

$ School of Applied and Engineering Physics, Cornell University, Ithaca, New York 14853, USA

$$ Department of Biochemistry, Bahauddin Zakariya University, Multan-60800, Punjab, Pakistan

$$$ SLAC

$$$$ Wiley

Abstract

Serial Crystallography at synchrotron light sources offers the possibility to routinely collect data at room temperature using micron sized crystals of biological macromolecules. However, it suffers from the fact that data collection is not yet as routine as the standard rotation series cryo-crystallography. Moreover, data collection times are currently significantly longer, impairing its use for high-throughput approaches, such as fragment-based drug screening. On the way to high-throughput serial synchrotron crystallography, we show here, using three different proteins that complete data sets for can be collected in less than a minute. We also demonstrate how sample-efficient and radiation damage free we can collect data.

Introduction

Differently from the fixed-axes X-ray crystallographic experiment, where typically a single crystal is rotated to collect a complete set of diffraction data, serial crystallography approaches achieve similar results by using a stream of microcrystals presented to the beam at random orientations[1]. Today, twelve years after the first successful serial crystallography experiments at the experimental station AMO at LCLS (SLAC, USA)[1], this method is being used not only at X-ray free-electron laser sources (XFEL), but also increasingly frequently at 'conventional' synchrotron radiation sources[2–9]. While serial data collection at synchrotron radiation sources (SSX) does not benefit from the 'diffract-before-destroy'-principle[10] exploited by XFEL serial femtosecond crystallography (SFX), the wide availability of

macromolecular crystallography (MX) experimental stations at synchrotrons worldwide has spurred interest to develop alternative approaches and explore possibilities for serial measurements. The X-ray intensities at 3rd and 4th generation synchrotron sources, such as PETRA III, NSLS II, MAX IV, APS, ESRF, SLS, Spring8, and Diamond Light Source, allow for exposure times of micron-sized crystals in the low ms to even µs-range[11], much longer than those at XFELs that are typically in the tens of femtoseconds range. While this limits time resolution of SSX compared to SFX, the use of polychromatic X-rays (pink beam) with 100 ps-long pulses has been used successfully for SSX data collection[12]. Polychromatic serial Laue crystallography offers the benefit that a full data set can be achieved in only about 50 crystal exposures, making this approach extremely fast and efficient in regard to sample consumption per dataset[12]. Moreover, the short exposure times offer the benefit that sample delivery methods used at XFELs, including liquid jets, can in principle be used for serial Laue crystallography, thus enabling fast mix-and-diffuse studies for time-resolved enzymology studies. Also, all other methods for triggering protein dynamics can be employed, as long as the desired time-resolution is not shorter than the single pulse length. With these improvements in efficient SSX, XFEL sources are best utilized for extremely small crystals, proteins containing heavy atoms (increasing their susceptibility to primary radiation damage), and ultra-fast processes that are faster than the exposure times at synchrotron sources.

The downside of serial Laue crystallography is a) the tedious, still not automated data processing, especially for indexing and integration, and b) there are only a handful of experimental stations currently in operation that have the capability to perform such experiments. On the other hand, there are many tens of monochromatic MX beamlines in operation. Here, time resolution is limited to the sub-ms range, due to the at least 1000-fold reduction in X-ray intensity, as compared to polychromatic X-rays. This still allows for many enzymatic reactions to be followed by means of time-resolved crystallography, either by light activation of photocaged substrates[13], mix-and-diffuse methods[3,14], or other triggering methods. Ideally, crystals can be as small as the X-ray spot size, which with the advent of diffraction limited sources and their loss-free achievable beam sizes, will allow for diffraction data collection from sub-micron sized crystals, enabling both more advanced and efficient mix-and-diffuse and light triggering methods. However, the longer exposure times do not permit the use of liquid jets for sample delivery, since these are too fast for useful diffraction data to be recorded from single crystals. For serial synchrotron crystallography, other methods originally developed for SFX have been used, such as viscous extrusion (LCP and other matrices)[6,7,15], fixed targets[4,16,17] or hybrid methods such as conveyor belt-based methods[3]. The advantages and disadvantages for each of these methods have been discussed extensively in literature,[18–21] and it is clear that each of these approaches has specific applications where it is the superior method. All of these methods still require specialized equipment and can be challenging to operate. Serial crystallography is not yet a standard method, even though, by design, it should be the method of choice at high intensity sources, where otherwise both photon flux and modern detectors are not put to full use. What hinders its broad use, is the fact that in most cases experts are still needed to successfully run the experiment. The CFEL TapeDrive (Figure 1), developed at DESY,[3] offers the possibility to enable straightforward serial synchrotron crystallography. Sample consumption is low (200-2000 nl/min), it is compatible with mix-and-diffuse methods for substrate or drug design studies, and since it does not require any modifications to the sample for sample delivery purposes, in the current setup, the sample vial can be plugged directly into the liquid dispensing system, without the need to transfer the sample, thus reducing the dead volume to about 5 µl (Figure

1). With this setup, efficient, high output serial synchrotron crystallography at room temperature is possible, not only for model proteins such as lysozyme as reported previously[3], but also for target proteins. Here we demonstrate this with three test cases: an Aspergillus flavus urate oxidase (UOX), *Nectria haematococca* xylanase (NhGH11)[22] and a CTX-M-14 β-lactamase[23] from *K. pneumoniae*. The CTX-M-14 β-lactamase from *K. pneumoniae* belongs to the extended spectrum β-lactamases (ESBLs) that play an important role in emerging multi-antibiotic resistance mechanisms. This class of enzymes is able to hydrolyze the β-lactam ring structure of most prominent antibacterial agents used in medicine and render them ineffective. The constantly evolving resistance to penicillin and penicillin-derived antibiotics is forcing the development of new antibiotics, as particular ESBLs, including CTX-M-14 from *K. pneumoniae,* are already able to cleave antibiotics specifically developed against pathogens with high β-lactamase stability, including third-generation cephalosporins, such as cefotaxime or ceftazidime. The NhGH11 xylanase is a highly active xylanase suitable for industrial applications, as shown by structural and biochemical studies[22] and UOX. Here we present the first room temperature structure of NhGH11 xylanase, the first room temperature structure of CTX-M-14 β-lactamase from *K. pneumoniae* without an inhibitor present, and a detailed investigation of the shortest data collection times, approaching the speed of single crystal cryo MX. In case of UOX a full dataset was collected from five crystals grown for cryo MX, showing sample efficiency of the TapeDrive system. Moreover, comparison with low exposure room temperature data collection using large crystals, shows the advantage of using room temperature SSX for radiation sensitive crystals.

Methods

Sample preparation

K. pneumoniae CTX-M-14 β-lactamase (CTX-M-14)

CTX-M-14 was produced, purified and crystallized as before[23], with a slight modification in crystallization conditions to obtain slightly bigger crystals which roughly match the X-ray focal spot. For this purpose, a 50% CTX-M-14 solution (22 mg/ml) was mixed with a 45% precipitant solution (40% PEG8000, 200 mM lithium sulfate, 100 mM sodium acetate, pH 4.5) and with a 5% undiluted seed stock in batch crystallization setups, resulting in crystals with a homogeneous size distribution of 11-15 µm after 90 minutes. The crystals were centrifuged at 200xg for 5 min and the supernatant was replaced with a stabilization buffer (28% PEG8000, 140 mM lithium sulfate, 70 mM sodium acetate, pH 4.5) to stop further crystal growth. Prior to the measurements, the microcrystal suspension was filtered using a 30 µm gravity flow filter (Celltrics, Sysmex).

Nectria haematococca xylanase (GH11)

GH11 was produced and purified as described previously[22]. For crystallization, the original conditions were modified to obtain microcrystals. Initial crystals obtained from hanging drops under the precipitant condition: 1 M ammonium sulfate, 100 mM sodium citrate pH 5.5 were crushed under a stereomicroscope, using a crystal crusher tool (Hampton research). The reservoir solution was pipetted to the drop and the seed stock was collected by washing the drop with reservoir solution. The seed stock was transferred to a seed bead tube (Molecular Dimensions Ltd., UK), vortexed three times for 30 s each, with an interval of 30 s between each vortex, to get the final seed stock. Protein solution 15 mg/mL, precipitant solution, and seed stock were mixed with a ratio of 1:1:0.5. The mixture was vortexed for 30 s in ten-minute intervals. After 30 min, the microcrystals were centrifuged at 200 rpm and the supernatant was replaced with a precipitant solution.

Applying the same protocol, microcrystals were obtained under two precipitant conditions i.e. Precipitant 1: 1M (NH4)2SO4, 100 mM sodium citrate pH 5.5, and Precipitant 2: 200 mM (NH4)2SO4, 100 mM sodium citrate pH 5.5 and 20% PEG 6000. Microcrystals obtained under both precipitant conditions were tested for diffraction data collection.

Aspergillus flavus urate oxidase (UOX)

Untagged UOX was expressed in *E. coli* using a codon-optimised synthetic cDNA (Genscript, USA) inserted into a pET24b vector. Protein expression was performed in *E.coli* BL21(DE3) cells at 20°C for ~20 hours. Protein purification was achieved using a combination of ammonium sulphate precipitation, DEAE and Resource Q ion exchange, Phenyl Sepharose hydrophobic interaction, and Superdex 75 size-exclusion chromatographic steps. For crystallization, UOX in Tris-acetate buffer (50 mM, pH 8.0) was concentrated to 20 mg/ml and saturated with 9-methyl uric acid (MUA). Large crystals were obtained at room temperature using the batch method by mixing the protein solution with a 8% PEG 8000 reservoir in a 1:2 ratio under aerobic conditions. With this method UOX crystals typically reach dimensions of at least 400×400×300 μm^3. In the presence of O_2 (air) UOX-bound MUA undergoes dioxygenation affording the mechanistically-relevant 5PMUA peroxide derivative[24]. The latter is stable in the crystal for approximately two/three weeks. For the SSX experiment, a total of five large crystals of the UOX-5PMUA complex (approximate dimensions 800x400x400 µm) were vortexed in the presence of 1 mm diameter glass beads for about 10 minutes and then diluted in their mother liquor to yield 1 ml microcrystalline suspension with crystal sizes in the 3-20 µm range. We did not experimented with bead-size but considered 1 mm beads a suitable choice as a previous report that used fragmentation for transmission electron microscopy (TEM) analysis indicated that the use of 0.5 and 1.0 mm beads resulted in homogeneous populations of crystal fragments of low-micrometre sizes[25]. The same study found that the standard 3.0 mm bead yielded inhomogeneous fragmentation with large crystal sizes still present in the solution whilst smaller beads (0.1 mm) produced no UV-detectable crystals. Following fragmentation, we passed the microcrystalline slurry through a 30 µm mesh-size filter (CellTrics, Sysmex), resuspended and otherwise used as is.

Beamline setup

For sample delivery, a conveyor belt apparatus, known as the TapeDrive[3], was used as described previously (Figure 1). However, in order to minimize the dead volume of the sample and to make sample delivery more efficient, the sample was directly pressurized by the ElveFlow system. The sample vial (Eppendorf, Germany), in which the protein was crystalized, was connected to the Elveflow OB1 flow controller using a special adaptor available from ElveSys.. A microfluidic flow sensor was also installed to control the flow rate. For mix-and-diffuse experiments the set-up was duplicated at a second channel at the Elveflow OB1 flow controller. The other side of the flow meter was connected to a Kapton-coated borosilicate capillary with an internal diameter of 180 µm (Polymicro, USA), through which the microcrystal suspension flowed onto the tape. This capillary can easily be swapped out for a mixing dispenser as described previously[3]. The end of the capillary that was in contact with the tape was sharpened for optimized sample flow onto the tape. The tape under the sample capillary was continuously moving, producing a sample stream on the tape that was aligned with the X-ray focus. As before, nonsticky polyimide tape with a width of 6 mm and a thickness of 12 µm (Caplinq, The Netherlands) was used. The tape position was vertically confined by grooves in the tape-drive body that matched the width of the tape. The TapeDrive was mounted to the crystallography endstation at the P11 beamline at PETRAIII (DESY, Hamburg),

such that the 12.0 keV photon energy X-rays were focused at sample position to a spot of 9 × 5 µm (width × height) with a maximum flux of about 1.6×10^{13} photons/s. To control X-ray exposure to the crystals, a rotating beam chopper made of a 4 mm thick brass plate with holes for the X-rays to pass through was placed upstream of the focusing optics. The signal from a photodiode placed downstream of the chopper was used to trigger the readout of a PILATUS 6M detector, resulting in the collection of one diffraction image per pulse. HiDRA was used to transfer data rapidly to the ASAP3 storage system at PETRAIII and the incoming data stream was monitored with OnDA[26] for fast feedback during the experiment. The online hit-finding parameters were optimized to beamline set-up and sample properties on the fly.

Data collection parameters were directly controlled in Tango/JIVE. One run consisted of a maximum of 40,000 diffraction images, for technical reasons. Data was collected at room temperature from randomly oriented microcrystals suspended in their crystallization buffer. For the first run of microcrystals of β-lactamase CTX-M-14 from *K. pneumoniae* the flow rate of sample was set to 2 µl/min. In all later runs discussed here, a stable sample flow rate of 1 µl/min was maintained.

Data processing

Data processing, starting directly from the native CBF-files, was carried out using the CrystFEL[27,28] 0.8.0 package. In indexamajig, the option --peaks=peakfinder8 was used to identify individual `hits' from the complete set of collected diffraction patterns. The complete set was defined by an automatically generated list of files. Detected `hits' were then indexed using Xgandalf[29], XDS[30], mosflm[31], asdf, and DIRAX[32] (in that order), and integrated with --int-radius=3,4,8 option. The geometry input file was adapted for the photon energy and detector distance from previous experiments at P11. For CTX-M-14, the resulting unmerged streams of indexed and integrated diffraction data was then processed with ambigator[33] in CrystFEL to resolve the indexing ambiguity. This was required as CTX-M-14 crystallizes in the enanthiomeric $P3_221$ space group, and thus exhibits indexing ambiguities. Scaling and merging of the data were carried out for all samples in partialator in CrystFEL using three iterations and the --push-res=2 option. MTZ files for crystallographic data processing were generated from CrystFEL merged reflection datafiles using F2MTZ within the CCP4[34] suite. Figures of merit were calculated using compare_hkl (R_{split}, $CC_{1/2}$ and CC*) and check_hkl (SNR, multiplicity and completeness), which are both part of CrystFEL.

Structure solution and refinement

For β-lactamase CTX-M-14 from *K. pneumoniae,* the structure determined at the European XFEL (6GTH)[23] was used as the initial model (after removal of the ligand, Avibactam). Owing to non-isomorphism of the collected data sets with that of 6GTH, R_{free} flags were generated randomly using phenix.refine[35,36], and the same set of R_{free} flags was then used for all data sets. Initial refinement was carried out using phenix.refine, with all isotropic atomic displacement parameters (ADPs) set to 20 Å^2 and using simulated annealing. Ions and ordered solvent molecules were built into the model using Coot, TLS-groups were identified using the TLSMD-server[37]. Iterative cycles of restrained maximum-likelihood and TLS refinement using phenix.refine and manual model rebuilding using Coot[38] were carried out until convergence. Polygon, MolProbity,[39] and thorough manual inspection were used for validation of the final model.

For NhGH11, we processed data with CrystFEL as described above, with the addition that in partialator we used both the “unity” and the “xsphere” partiality model, for comparative reasons. The cryo MX structure (PDB accession code: 6Y0H) of NhGH11[22] was used as the initial model and refinement was carried out essentially as described above, but without TLS-refinement. For the detailed investigation of the relation of data quality and length of data collection/indexed patterns, phenix.refine was used with exactly the same parameters and without manual intervention.

The room temperature SSX structure of the UOX-5PMUA complex was solved using the molecular replacement (MR) method starting from the model of the same complex obtained at near-atomic resolution under cryo-conditions and using low X-ray dose data (PDB code 4CW2) [24]. Prior MR the model was stripped of the bound ligand and all ordered solvent molecules. Crystallographic refinement was carried out using *Refmac*5 of the CCP4 suite[40,41]. Restraints for the bound 5PMUA molecule were generated using a recent version of AceDRG[42] now available in the latest CCP4 release 8.0. AceDRG derives atom types from the Crystallography Open Database[43].

PyMol, ChimeraX and coot[38] were used for the generation of molecular images. For RMSD calculations and alignment PyMol and ChimeraX[44] were used. Solvent channels and solvent channel maps for CTX-M-14 β-lactamase were calculated using map_channels[45].

Results

CTX-M-14 β-lactamase

For CTX-M-14 β-lactamase we collected an initial SSX data set of 10’000 diffraction images in 400 s (dataset 10K). We had originally planned a longer data collection but X-ray loss due to a beam dump at PETRAIII prevented its further progression. Nevertheless, this ‘mini data set’ afforded a total of 4286 indexed images from only about 13.3 µl of sample injected. This 42.9 % `indexing fraction' of the total collected detector exposures, corresponds to an effective data collection rate of about 10.7 Hz with only 32.2 ng of protein consumed per indexable detector frame. Processing with the CrystFEL package indicated that these 4286 indexed frames already constituted a complete dataset to about 1.55 Å resolution with excellent statistics (Table 1). Crystallographic refinement indicators and the resulting electron density maps further confirmed the high quality of the data.

Based on this ‘accidental’ observation of the possibility to collect a complete SSX dataset in little more than six minutes, we carried out a more systematic investigation. Three more independent runs with microcrystals of β-lactamase CTX-M-14 were collected, yielding 61’331 indexable detector frames from a total of 127’171 recorded frames (dataset “all”). This corresponds to a 48.2 % average `indexing fraction' with 28.7 ng of protein consumed per indexable detector frame and a total volume of 91.4 µl of microcrystalline suspension used. Data collection and refinement statistics are, as expected, superior for the combination of all runs, and the nominal resolution (based on a $CC_{1/2}$ cut-off of 0.15) extends to 1.4 A (in comparison to 1.55 A for the rapid data collection). This improvement in statistics is not clearly visible in the electron density (see Figure 2). We then looked at the first 5000 frames collected in the first run (dataset 5K). At 25 Hz (maximum frame rate of the Pilatus 6M) this corresponds to a total of 200 s of X-rays or 3:20 minutes of data collection time. From these 5000 images, 5109 crystals could be indexed with CrystFEL and data collection statistics show that with these 5109 indexed crystals, a full dataset to about 1.55 A resolution can be obtained, meaning

that less than three and a half minutes of data collection time is needed to obtain a full serial crystallography data set to near-atomic resolution using monochromatic X-rays at a synchrotron. For these 5109 indexed crystals, a total of no more than 34 ug of protein in roughly 3.3 µl of microcrystalline suspension were used. This corresponds to only 6.65 ng protein consumed per indexable detector frame. In comparison: 6250 ng were used in the first serial synchrotron crystallography experiment and 89 ng in the lysozyme mix-and diffuse study. Again, the refinement statistics and the resulting electron density maps are of excellent quality (see table 1 and figure 2).

The CTX-M-14 crystals used here had the same symmetry and unit cell parameters as the microcrystals in complex with avibactam used at EuXFEL[23] and thus differ from the larger crystals with and without inhibitors grown under similar conditions and used for single crystal MX at cryogenic conditions[46]. The datasets collected here were used to determine the first non-cryogenic structures of an inhibitor-free CTX-M-14 β-lactamase from *K. pneumoniae.* Whereas the crystal contacts and symmetry are completely different from the corresponding cryogenic structure[46] (PDB accession code: 7Q0Z), the structures are very similar (RMSD of 0.332 A, Figure 3 and Figure S1), albeit a bit larger than the RMSD between the structures from different numbers of indexed crystals from this study ("all" vs. 10K: 0.091 A, "all" vs. 5K: 0.085 A, 10K vs 5K: 0.093 A). The RMSDs between the structure from EuXFEL[23] (PDB accession code: 6GTH) and the structures from this study lay in between and range from 0.161 A (EuXFEL vs "all") to 0.166 A (vs 5K) and 0.169 A (vs 10 K). Just as in the EuXFEL structure two N-terminal residues that could be built in the cryogenic structure (E25 and T26) could not be built in all three RT-SSX structures due to the absence of interpretable electron density. On the other hand, an additional residue (L289) could be built into electron density in all three datasets from this study. A residue that was absent in both the EuXFEL and the cryogenic structure. The different packing of the crystals in the cryogenic case and the microcrystal RT cases also results in a slightly different solvent accessibility within the crystal. Using the tool map_channels[45] we calculated solvent channels within the crystals and indeed the channels for the microcrystals at rt are slightly larger than those in the larger crystals used for cryoMX, making mix-and-diffuse studies theoretically more feasible (see Figure S2). The B-factors and Wilson B of all rt structures are very similar and – as expected - higher than those of the structure refined against data collected under cryogenic conditions. Interestingly – between the RT-SSX datasets - the Wilson B is lowest in the 5K-dataset, indicating that the accuracy of the determination of intensity values is rather independent of the addition of more indexed images to integration and merging and that around 5000 indexed crystals give sufficiently accurate intensity values.

NhGH11

For NhGH11, a run, consisting of 40'000 detector images was collected (26 minutes and 40 seconds run duration). The run was split into 40 datasets, each consisting of 1000 detector images, and processed with the CrystFEL pipeline separately and treated as 40 individual datasets, to look at fluctuations in data quality and indexing rate. Next, 1000, 2000, 3000, 4000, 5000, 6000, 8000, 10'000, 15'000, 20'000, 30'000, and finally all the 40'000 detector images were processed together in partialator to assess the number of indexed images needed for a full dataset. Going from 1000 images to 40'000 images the resolution at which CC* reaches 0.5 (the typical cut-off level in macromolecular crystallography) goes from 1.83 A down to 1.5 A (see Figure 4A). Using the same parameters in phenix.refine and a high-resolution cut-off at 1.9 A, R_{free}-values drop from 0.264 (1000 images) to 0.166 (40'000

images). The improvement in reasonable resolution and R_{free} with the addition of more images merged, however, is not uniform, as can be seen in Figure 4 B. R_{free} drops from 0.264 to 0.22, 0.21 and 0.189 respectively when merging 4000, 5000 and 10'000 instead of 1000 detector images and only drops further to 0.166 for the full run (40'000 images). Similarly, the resolution at which CC* of the highest resolution shell reaches 0.5 drops from 1.83 to 1.65 by using 4000 instead of 1000 images, and only drops to 1.58 A at 10,000 images and 1.50 A at 40'000 images (Figure 4A). Similar progress can be seen when looking at overall values of CC*or R_{split} (Figure 4 C and D). Improvement in data quality can best be assessed when looking at the evolution of electron density maps with the addition of more indexed detector frames (Figure 5). Here maps generated from automatic refinement (uniform resolution cut-off at 1.9 A, same input mode, same parameters, see Figure 4B for corresponding R_{work} and R_{free}) around Tyr41 are shown and clear improvement of map quality with the addition of more detector images can be seen.

When looking at the 40 datasets, each consisting of 1000 detector images, within these datasets there is no clear trend, neither for the number of indexable patterns per frame, nor for the values for R_{free} after automatic refinement. The indexing rate ranges from 91.5 % to 121.5 % and R_{free} values from 0.259 to 0.306, and the number of indexable frames and resulting R_{free} are not clearly correlated (Figure 6).

Partiality refinement in CrystFEL partialator with the xsphere-partiality model was also used, to assess if improvements could be seen especially for the case of using only 1000 images per dataset. In all 40 individual 1000 image datasets the data quality metrics (R_{split}, CC*, $CC_{1/2}$, SNR) improved when using partiality refinement (Figure 6, B-D). In most cases the quality improvement was quite uniform across the 40 datasets, i.e. similar relative changes upon partiality refinement. Over all 40 datasets CC* went up by 0.0289 ± 0.0069 (from 0.9100 ± 0.0093 to 0.9388 ± 0.0079). However, there were some outliners, for example dataset 30, where overall SNR improved from 1.74 to 3.40, and overall $CC_{1/2}$ changed from 0.71 to 0.81. Using automated refinement with the same conditions across all datasets for both conditions (with and without partiality modelling) the improvement through partiality refinement was less clear as indicated by the crystallographic metrics. In some cases R_{work} and R_{free} did not improve for the same dataset after partiality modeling in CrystFEL, however this was only true for 15% of the cases (six in total). In one case the R_{free} remained the same and in 82.5% there were slight improvements through partiality modelling. The average R_{free} over all 40 datasets dropped by 0.006 ± 0.001 (from 0.281 ± 0.002 to 0.275 ± 0.002) and the average R_{work} dropped by 0.004 ± 0.001 (from 0.243 ± 0.002 to 0.239 ± 0.001).

The high and relatively uniform indexing rate and the absence of a trend in crystallographic or refinement statistics implies that – for these crystals at least – settling or other negative effects over the duration of one run cannot be observed and that the TapeDrive can be used for stable and carefree data collection.

Already for the CTX-M-14 β-lactamase we could observe that the Wilson B-factor and the ADP from refinement are rather independent of the number of indexed crystals in a dataset. Here we could extend this investigation to the range from 1000 to 40'000 detector images. Using the same refinement strategy and input PDB the average isotropic ADP drops slightly from 23.4 (1000 images) to 22.8 (40'000 images), however, again no clear trend is visible, with the ADP being at 23.4 using 30'000 detector images (Figure S3).

In the case of *Nectria haematococca* xylanase the crystal symmetry does not change with the change of crystal size. The crystals used for cryoMX[22] (PDB accession code: 6Y0H) are almost isomorphous to those used in this RT-SSX study, with the latter ones having slightly larger unit cells (a=80.55, b=38.85, c=53.57, alpha=90, beta=91, gamma=90 (rt) vs a=79.45, b=38.50, c=53.59, alpha=90.00, beta=91.43, gamma=90.00 (cryo)). The structural models resulting from refinement against the RT-SSX datasets are the first room temperature datasets of this *Nectria haematococca* xylanase. The structures superimpose very well with the structure from cryoMX (C_α-RMSDs ranging from 0.226 A for the 1000 images dataset to 0.213A for the 40'000 images dataset, Figure 7) and differences are mostly visible in the orientations of sidechains. The two catalytic residues E89 and E180 overlap perfectly in their entirety, with an all-atom RMSD of 0.126 A (Figure 7). The alignment of all the residues of the active site (S19, W21, Y76, Y80, E89, Y91, P101, R125, Q139, Y174, E180 and Y182) is slightly worse, with an all-atom RMSD of 0.519 A and comparable with the all-atom RMSD of all the residues (0.583 A). The same alignment carried out using the 1000 image dataset, instead of the 40k dataset resulted in a slightly worse all atom RMSD of 0.630 A (Figure 8). For just the two catalytic residues E89 and E180 the all atom RMSD is 0.151 A, overall the residues in the active site align very well in all three cases (Figure S4). This shows, that a) the addition of more images in a SSX dataset increases – as excpected - the accuracy of the resulting model, but also b) that the improvements, given the 40 times longer data collection time, are rather minor and that useful models even for mechanistic studies can be generated from refinement against datasets made by merging of just 1000 detector images, corresponding to 40s data collection time. In the case of NhGH11 the same number of residues could be built into electron density in all RT-SSX datasets and there are no differences to the cryoMX structure.

UOX-5PMUA complex

Differently from the other experiments discussed here, in the case of the UOX-5PMUA complex no attempt was made to grow microcrystals. Instead, we purposefully crushed five large crystals (approximate volume, 0.13 mm^3) using 1-mm diameter glass beads to explore whether this rather coarse approach could be useful for SSX experiments when, for example, microcrystal optimization is problematic. Using this method, we collected a total of 170905 frames with 3142 patterns indexed successfully. This low percentage (1.84%) is entirely due to the high dilution of the crystal slurry used that resulted in a very high number of empty frames. The number of indexed patterns matched the number of crystals indicating that all microcrystals were successfully indexed and that there were no 'multiple hits'. Overall, this approach afforded, after merging, a complete 2.3-Å resolution data set that was employed to determine the structure of the UOX-5PMUA complex at room temperature. Data collection and refinement statistics are reported in Table 1.

One of the strengths of serial crystallography approaches is their reduced impact on radiation-sensitive samples as the absorbed dose is spread over many crystals. This is particularly relevant at room temperature where the absorbed dose that induce global radiation damage can be two orders of magnitude lower than those at cryogenic temperatures[47,48]. Our previous work has shown that the C5-O1 bond of 5PMUA (highlighted in red in Figure XA) is extremely susceptible to radiolysis. At 100 K, we have observed that an average diffraction-weighted dose (DWD) of about 200 kGy results in virtually the complete rupture of the C5-O1 bond and values as low as 2.5 kGy are required to minimize this[24,49]. Specific radiation damage in 5PMUA manifests itself with the development of negative density peaks in difference Fourier maps

along the C5-O1 bond reflecting its rupture whilst positive density appears in the heterocyclic plane because of the loss of pyramidalization at C5 with this carbon atom transitioning from sp^3 to sp^2 hybridisation. Concomitantly, dioxygen is liberated from the peroxide moiety and, at cryo-temperatures, remains trapped above it.

The present SSX experiment offered the opportunity to study the UOX-5PMUA complex at room temperature. Already at the initial stage of model refinement, difference Fourier maps revealed unambiguously that MUA had reacted with O_2 to produce the 5PMUA adduct in the crystal (Figure XB). As previously seen in the structure of the complex solved at cryo-temperature, 5PMUA binds at the interface between two protomers of the UOX tetrameric assembly in a cavity lined by K10*, I54*, A56*, T57*, D58*, F159, R176, L170, S226, V227, Q228, N254, H256, G286, I288 (the asterisk indicates residues belonging to a separate UOX chain) with the peroxide moiety sandwiched between the side-chains of T57* and N254.. Inspection of electron density maps obtained from the SSX experiment does not reveal signs of obvious 5PMUA radiolysis (Figure XC). The peroxide moiety displays pronounced pyramidalization at C5 accompanied by the strong distortion of its fused heterocycles. The C5-O1 bond length refines at the target value of 1.44 Å with none of the hallmarks of C5-O1 rupture visible in mF_o-DF_c maps at the $\pm 3\sigma$ level. Lowering the contour level we observe some negative density along the C5-O1 bond at $\pm 2.5\sigma$, however, this is matched by similar peaks in other regions of the maps thus suggesting that noise is a contributing factor at this threshold. Exact dose calculations are not straightforward for the present TapeDrive experiment because of complicating factors such as non-homogenous crystal size and variable crystal positioning with respect to the Gaussian-shaped beam. Nonetheless, DWD estimation using Raddose-3D[50,51] provides a value of approximately 70 kGy as an upper limit. The Raddose-3D script used for the calculation is available in the supplementary material.

Overall, the quick 'crush-and-collect' approach employed here allowed the determination of the room-temperature structure of the UOX-5PMUA complex and the visualization of the radiation-sensitive 5PMUA intermediate without obvious signs of specific radiolysis.

Conclusion and Discussion

Serial crystallography has made tremendous progress in the past five years, especially for its use at synchrotron light sources. It has brought back data collection at room temperature and revived time-resolved approaches to track structural dynamics of biological macromolecules. The conveyor-belt based TapeDrive combines – as a hybrid approach – the advantages of fixed target and liquid jet-based sample delivery. Here, we showed that sample consumption per dataset using this system is *en par* or even lower than with fixed target or viscous extrusion approaches. At the same time the TapeDrive system allows for uninterrupted data collection without manual intervention or the need to enter the hutch. Moreover, it enables future automated multi-parameter data collection for multidimensional serial crystallography[52]. This was demonstrated by collecting 40 datasets in less than 30 minutes, wherein each dataset has good statistics and usable diffraction to a resolution of better than 2A and each of the datasets took 40 s to collect with a Pilatus 6M detector, corresponding to only 7.5 s using an Eiger 16M at 133 Hz. More notably: in this setting less than 5 ug of protein were used per dataset, which would drop to below 1 µg of protein per dataset using the EIGER instead of the PILATUS. If a higher resolution is desired, longer data collection times improve resolution, i.e. recording more indexable detector images, with a sweet spot – in this case – at roughly 4000 images. However, looking at the resulting models and the accuracy of the positions of the active side

residues of NhGH11 (Figure 8), the differences between the datasets from 40'000 respectively 1000 recorded detector images are rather marginal and the 40 times longer data collection time and 40 times higher sample consumption is not justified by the improvement. For further improvement, without using more sample or data collection time, the partiality refinement option in CrystFEL can be used, which - for small datasets – does not slow down data processing. In this study it improved crystallographic statistics across all 40 datasets, even though the effect on the refinement statistics was not that uniform and its use has to be assessed on a case-to-case basis.

SSX experiments require the production of homogenous micro-crystals. Strategies have been proposed to reproducibly achieve this by modifying the conditions used to produce single well-ordered crystals, that are typically the focus of most crystallographic laboratories [44]. While the correct understanding of the crystallization phase diagram is undoubtedly beneficial to facilitate the macrocrystal-to-microcrystal transition, the intrinsically complex nature of biological crystal formation suggests that this can be a time-consuming process. Fragmentation of large, imperfect crystals into microcrystals or nanocrystals has been used for the structure determination of various test proteins by the electron cryo-microscopy (cryo-EM) method of microelectron diffraction (microED)[53]. Here, we employed the rather crude approach of crushing large crystals to SSX. In the case of the UOX-5PMUA complex this allowed to obtain a complete data set at 2.3 Å-resolution with satisfactory diffraction statistics. At present, we are unable to comment on how the quality of these crushed microcrystals compares with that of 'grown-for-purpose' ones, although the latter will provide a more homogenous population that will be beneficial for mix-and-diffuse studies. Nonetheless, our experiment with UOX-5PMUA shows that should micro-crystal optimization be problematic this is not necessarily a showstopper and crushing standard-size crystals can be attempted if enough are available. It is expected that the success of this will be very much dependent on the quality of the original crystals.

By their own nature, serial methods whether at synchrotrons or at XFELs distribute the absorbed energy over a multitude of crystals, instead of accumulating it as in oscillation-based data collections. This is particularly important at room-temperature where, compared to cryo conditions, radiation damage degrades data quality at much lower doses. Therefore, whilst not providing completely radiation-damage free data, serial approaches are able mitigate the negative impact of radiolysis in macromolecular crystallography[54,55]. In addition to global effects, loss of diffraction power being the most obvious one, radiation damage leads also to specific changes to biological molecules. For example, decarboxylation of acidic residues, rupture of disulfide bridges and geometric alterations at metal centres due to photoreduction are rather common effects[56–60].

In the case of the UOX-5PMUA complex, the radiolytic effect previously observed at cryo-temperatures is of C5-O1 bond breakage with concomitant flattening of the fused ring system and trapping of O_2 above it[24]. A dose (DWD) in the 50-100 kGy range already leads to visible effects. We were therefore quite surprised that the present SSX experiment did not reveal radiation-damage effects on PMUA considering that DWD was in the order of tens of kGy with an estimated upper limit of around 70 kGy. Clearly, we should not exclude the possibility that limited resolution and non-isomorphism induced by global radiation damage might swamp peaks in Fourier difference maps such that some specific damage is concealed. However, it appears unlikely that these effects can mask C5-O1 bond rupture completely also considering

that our dose is well below the rough limit of 380 kGy suggested to minimize global damage[54]. Previous studies have highlighted differences in radiation damage effects at room- and cryo-temperature with respect to S-S bond breakage and decarboxylation of acidic residues[54,61]. Particularly, intriguing is the observation that in lysozyme crystals Fourier difference maps at RT did not show damage at carboxyl groups of Glu and Asp residues, in contrast to what observed in cryo- control series[54]. Whilst various hypotheses can be put forward with respect to the apparent lack of damage of 5PMUA in the current SSX experiment including radical chemistry that facilitates recombination or possibly a dose-rate effect, further systematic investigations will be required to explore this in detail. Considering that crystallographic experiments at near physiological temperatures are becoming more common, a deeper understanding of radiation damage under these conditions is of uttermost importance.

In summary, the TapeDrive allows for seamless, rapid, efficient and radiation damage free data collection at synchrotron light sources. In this study the frame rate of the Pilatus 6M detector was the bottleneck for efficiency and the use of high framerate EIGER, LAMBDA or JUNGFRAU detectors will further improve this method and its usability as a standard tool for MX data collection, with data collection times and sample consumption per dataset reaching those for cryoMX at highly automated state-of-the-art beamlines. Having optimized samples, as was the case for NhGH11 and CTX-M-14 β-lactamase (an effort comparable to the optimization of crystals for cryoMX), between 500 and 1000 datasets could be collected within 12h. Since one tape roll lasts for more than 12h, one can collect these datasets without ever entering the hutch, fully automated and remote. Using an EIGER 16M at a framerate of 133 Hz instead of the PILATUS, up to 5400 datasets in 12h are possible, or, collecting 5000 detector images per dataset to be on the safe side, still more than 1000 datasets, which is slightly more than the number of datasets possible at high throughput cryoMX beamlines and certainly more than what is currently possible for SSX with fixed targets With this and further developments already under way, the TapeDrive will enable autonomous and high output data collection, from drug screening at physiological pH-values and temperatures, to combined temperature-, concentration-, time- and pH-resolved 7D multidimensional investigations.

Acknowledgments

We would like to thank Alke Meents and Kenneth Beyerlein for useful discussions, Juraj Knoska for helping out with capillaries, Yaroslav Gevorkov for support with XGandalf settings and Andre Rothkirch for assistance regarding data systems at PETRAIII. This research was supported in part through the Maxwell computational resources operated at Deutsches Elektronen-Synchrotron DESY, Hamburg, Germany. Some Figures were created with BioRender.com.

References

(1) Chapman, H. N.; Fromme, P.; Barty, A.; White, T. A.; Kirian, R. A.; Aquila, A.; Hunter, M. S.; Schulz, J.; DePonte, D. P.; Weierstall, U.; Doak, R. B.; Maia, F. R. N. C.; Martin, A. V.; Schlichting, I.; Lomb, L.; Coppola, N.; Shoeman, R. L.; Epp, S. W.; Hartmann, R.; Rolles, D.; Rudenko, A.; Foucar, L.; Kimmel, N.; Weidenspointner, G.; Holl, P.; Liang, M.; Barthelmess, M.; Caleman, C.; Boutet, S.; Bogan, M. J.; Krzywinski, J.; Bostedt, C.; Bajt, S.; Gumprecht, L.; Rudek, B.; Erk, B.; Schmidt, C.; Homke, A.; Reich, C.; Pietschner, D.;

Struder, L.; Hauser, G.; Gorke, H.; Ullrich, J.; Herrmann, S.; Schaller, G.; Schopper, F.; Soltau, H.; Kuhnel, K.-U.; Messerschmidt, M.; Bozek, J. D.; Hau-Riege, S. P.; Frank, M.; Hampton, C. Y.; Sierra, R. G.; Starodub, D.; Williams, G. J.; Hajdu, J.; Timneanu, N.; Seibert, M. M.; Andreasson, J.; Rocker, A.; Jonsson, O.; Svenda, M.; Stern, S.; Nass, K.; Andritschke, R.; Schroter, C.-D.; Krasniqi, F.; Bott, M.; Schmidt, K. E.; Wang, X.; Grotjohann, I.; Holton, J. M.; Barends, T. R. M.; Neutze, R.; Marchesini, S.; Fromme, R.; Schorb, S.; Rupp, D.; Adolph, M.; Gorkhover, T.; Andersson, I.; Hirsemann, H.; Potdevin, G.; Graafsma, H.; Nilsson, B.; Spence, J. C. H. Femtosecond X-Ray Protein Nanocrystallography. *Nature*, 2011, *470*, 73–77. https://doi.org/10.1038/nature09750.

(2) Stellato, F.; Oberthur, D.; Liang, M.; Bean, R.; Gati, C.; Yefanov, O.; Barty, A.; Burkhardt, A.; Fischer, P.; Galli, L.; Kirian, R. A.; Meyer, J.; Panneerselvam, S.; Yoon, C. H.; Chervinskii, F.; Speller, E.; White, T. A.; Betzel, C.; Meents, A.; Chapman, H. N. Room-Temperature Macromolecular Serial Crystallography Using Synchrotron Radiation. *IUCrJ*, 2014, *1*, 204–212. https://doi.org/10.1107/S2052252514010070.

(3) Beyerlein, K. R.; Dierksmeyer, D.; Mariani, V.; Kuhn, M.; Sarrou, I.; Ottaviano, A.; Awel, S.; Knoska, J.; Fuglerud, S.; Jonsson, O.; Stern, S.; Wiedorn, M. O.; Yefanov, O.; Adriano, L.; Bean, R.; Burkhardt, A.; Fischer, P.; Heymann, M.; Horke, D. A.; Jungnickel, K. E. J.; Kovaleva, E.; Lorbeer, O.; Metz, M.; Meyer, J.; Morgan, A.; Pande, K.; Panneerselvam, S.; Seuring, C.; Tolstikova, A.; Lieske, J.; Aplin, S.; Roessle, M.; White, T. A.; Chapman, H. N.; Meents, A.; Oberthuer, D. Mix-and-Diffuse Serial Synchrotron Crystallography. *IUCrJ*, 2017, *4*, 769–777. https://doi.org/10.1107/S2052252517013124.

(4) Schulz, E. C.; Mehrabi, P.; Müller-Werkmeister, H. M.; Tellkamp, F.; Jha, A.; Stuart, W.; Persch, E.; De Gasparo, R.; Diederich, F.; Pai, E. F.; Miller, R. J. D. The Hit-and-Return System Enables Efficient Time-Resolved Serial Synchrotron Crystallography. *Nat. Methods* **2018**, *15* (11), 901–904. https://doi.org/10.1038/s41592-018-0180-2.

(5) Botha, S.; Baitan, D.; Jungnickel, K. E. J.; Oberthur, D.; Schmidt, C.; Stern, S.; Wiedorn, M. O.; Perbandt, M.; Chapman, H. N.; Betzel, C. De Novo Protein Structure Determination by Heavy-Atom Soaking in Lipidic Cubic Phase and SIRAS Phasing Using Serial Synchrotron Crystallography. *IUCrJ*, 2018, *5*, 524–530. https://doi.org/10.1107/S2052252518009223.

(6) Botha, S.; Nass, K.; Barends, T. R. M.; Kabsch, W.; Latz, B.; Dworkowski, F.; Foucar, L.; Panepucci, E.; Wang, M.; Shoeman, R. L.; Schlichting, I.; Doak, R. B. Room-Temperature Serial Crystallography at Synchrotron X-Ray Sources Using Slowly Flowing Free-Standing High-Viscosity Microstreams. *Acta Crystallographica Section D Biological Crystallography*, 2015, *71*. https://doi.org/10.1107/s1399004714026327.

(7) Weinert, T.; Skopintsev, P.; James, D.; Dworkowski, F.; Panepucci, E.; Kekilli, D.; Furrer, A.; Brünle, S.; Mous, S.; Ozerov, D.; Nogly, P.; Wang, M.; Standfuss, J. Proton Uptake Mechanism in Bacteriorhodopsin Captured by Serial Synchrotron Crystallography. *Science* **2019**, *365* (6448), 61–65. https://doi.org/10.1126/science.aaw8634.

(8) Weinert, T.; Olieric, N.; Cheng, R.; Brünle, S.; James, D.; Ozerov, D.; Gashi, D.; Vera, L.; Marsh, M.; Jaeger, K.; Dworkowski, F.; Panepucci, E.; Basu, S.; Skopintsev, P.; Doré, A. S.; Geng, T.; Cooke, R. M.; Liang, M.; Prota, A. E.; Panneels, V.; Nogly, P.; Ermler, U.; Schertler, G.; Hennig, M.; Steinmetz, M. O.; Wang, M.; Standfuss, J. Serial Millisecond Crystallography for Routine Room-Temperature Structure Determination at Synchrotrons. *Nat. Commun.* **2017**, *8* (1), 542. https://doi.org/10.1038/s41467-017-00630-4.

(9) Martin-Garcia, J. M.; Conrad, C. E.; Nelson, G.; Stander, N.; Zatsepin, N. A.; Zook, J.; Zhu, L.; Geiger, J.; Chun, E.; Kissick, D.; Hilgart, M. C.; Ogata, C.; Ishchenko, A.; Nagaratnam, N.; Roy-Chowdhury, S.; Coe, J.; Subramanian, G.; Schaffer, A.; James, D.; Ketwala, G.; Venugopalan, N.; Xu, S.; Corcoran, S.; Ferguson, D.; Weierstall, U.; Spence, J. C. H.; Cherezov, V.; Fromme, P.; Fischetti, R. F.; Liu, W. Serial Millisecond Crystallography of Membrane and Soluble Protein Microcrystals Using Synchrotron Radiation. *IUCrJ* **2017**, *4* (4), 439–454. https://doi.org/10/gbnwdp.

(10) Chapman, H. N.; Caleman, C.; Timneanu, N. Diffraction before Destruction. *Philos. Trans. R. Soc. B Biol. Sci.* **2014**, *369* (1647), 20130313. https://doi.org/10/f23347.

(11) Nanao, M.; Basu, S.; Zander, U.; Giraud, T.; Surr, J.; Guijarro, M.; Lentini, M.; Felisaz, F.; Sinoir, J.; Morawe, C.; Vivo, A.; Beteva, A.; Oscarsson, M.; Caserotto, H.; Dobias, F.; Flot, D.; Nurizzo, D.; Gigmes, J.; Foos, N.; Siebrecht, R.; Roth, T.; Theveneau, P.; Svensson, O.; Papp, G.; Lavault, B.; Cipriani, F.; Barrett, R.; Clavel, C.; Leonard, G. ID23-2: An Automated and High-Performance Microfocus Beamline for Macromolecular Crystallography at the ESRF. *J. Synchrotron Radiat.* **2022**, *29* (2), 581–590. https://doi.org/10.1107/S1600577522000984.

(12) Meents, A.; Wiedorn, M. O.; Srajer, V.; Henning, R.; Sarrou, I.; Bergtholdt, J.; Barthelmess, M.; Reinke, P. Y. A.; Dierksmeyer, D.; Tolstikova, A.; Schaible, S.; Messerschmidt, M.; Ogata, C. M.; Kissick, D. J.; Taft, M. H.; Manstein, D. J.; Lieske, J.; Oberthuer, D.; Fischetti, R. F.; Chapman, H. N. Pink-Beam Serial Crystallography. *Nat. Commun.* **2017**, *8* (1), 1281. https://doi.org/10.1038/s41467-017-01417-3.

(13) Mehrabi, P.; Schulz, E. C.; Dsouza, R.; Müller-Werkmeister, H. M.; Tellkamp, F.; Miller, R. J. D.; Pai, E. F. Time-Resolved Crystallography Reveals Allosteric Communication Aligned with Molecular Breathing. *Science* **2019**, *365* (6458), 1167–1170. https://doi.org/10.1126/science.aaw9904.

(14) Mehrabi, P.; Schulz, E. C.; Agthe, M.; Horrell, S.; Bourenkov, G.; von Stetten, D.; Leimkohl, J.-P.; Schikora, H.; Schneider, T. R.; Pearson, A. R.; Tellkamp, F.; Miller, R. J. D. Liquid Application Method for Time-Resolved Analyses by Serial Synchrotron Crystallography. *Nat. Methods* **2019**, *16* (10), 979–982. https://doi.org/10.1038/s41592-019-0553-1.

(15) Nogly, P.; James, D.; Wang, D.; White, T. A.; Zatsepin, N.; Shilova, A.; Nelson, G.; Liu, H.; Johansson, L.; Heymann, M.; Jaeger, K.; Metz, M.; Wickstrand, C.; Wu, W.; Båth, P.; Berntsen, P.; Oberthuer, D.; Panneels, V.; Cherezov, V.; Chapman, H.; Schertler, G.; Neutze, R.; Spence, J.; Moraes, I.; Burghammer, M.; Standfuss, J.; Weierstall, U. Lipidic Cubic Phase Serial Millisecond Crystallography Using Synchrotron Radiation. *IUCrJ*, 2015, *2*. https://doi.org/10.1107/s2052252514026487.

(16) Roedig, P.; Duman, R.; Sanchez-Weatherby, J.; Vartiainen, I.; Burkhardt, A.; Warmer, M.; David, C.; Wagner, A.; Meents, A. Room-Temperature Macromolecular Crystallography Using a Micro-Patterned Silicon Chip with Minimal Background Scattering. *J Appl Crystallogr*, 2016, *49*, 968–975. https://doi.org/10.1107/S1600576716006348.

(17) Sherrell, D. A.; Lavens, A.; Wilamowski, M.; Kim, Y.; Chard, R.; Lazarski, K.; Rosenbaum, G.; Vescovi, R.; Johnson, J. L.; Akins, C.; Chang, C.; Michalska, K.; Babnigg, G.; Foster, I.; Joachimiak, A. Fixed-Target Serial Crystallography at Structural Biology Center. bioRxiv April 6, 2022, p 2022.04.06.487333. https://doi.org/10.1101/2022.04.06.487333.

(18) Grünbein, M. L.; Nass Kovacs, G. Sample Delivery for Serial Crystallography at Free-Electron Lasers and Synchrotrons. *Acta Crystallogr. Sect. Struct. Biol.* **2019**, *75* (2), 178–191. https://doi.org/10/gmptnt.

(19) Martiel, I.; Müller-Werkmeister, H. M.; Cohen, A. E. Strategies for Sample Delivery for Femtosecond Crystallography. *Acta Crystallogr. Sect. Struct. Biol.* **2019**, *75* (2), 160–177. https://doi.org/10/gmptns.

(20) Oberthuer, D.; Knoska, J.; Wiedorn, M. O.; Beyerlein, K. R.; Bushnell, D. A.; Kovaleva, E. G.; Heymann, M.; Gumprecht, L.; Kirian, R. A.; Barty, A.; Mariani, V.; Tolstikova, A.; Adriano, L.; Awel, S.; Barthelmess, M.; Dorner, K.; Xavier, P. L.; Yefanov, O.; James, D. R.; Nelson, G.; Wang, D.; Calvey, G.; Chen, Y.; Schmidt, A.; Szczepek, M.; Frielingsdorf, S.; Lenz, O.; Snell, E.; Robinson, P. J.; Sarler, B.; Belsak, G.; Macek, M.; Wilde, F.; Aquila, A.; Boutet, S.; Liang, M.; Hunter, M. S.; Scheerer, P.; Lipscomb, J. D.; Weierstall, U.; Kornberg, R. D.; Spence, J. C.; Pollack, L.; Chapman, H. N.; Bajt, S. Double-Flow Focused Liquid Injector for Efficient Serial Femtosecond Crystallography. *Sci Rep*, 2017, *7*, 44628. https://doi.org/10.1038/srep44628.

(21) Sierra, R. G.; Weierstall, U.; Oberthuer, D.; Sugahara, M.; Nango, E.; Iwata, S.; Meents, A. Sample Delivery Techniques for Serial Crystallography. In *X-ray Free Electron Lasers: A Revolution in Structural Biology*; Boutet, S., Fromme, P., Hunter, M. S., Eds.; Springer International Publishing: Cham, 2018; pp 109–184. https://doi.org/10.1007/978-3-030-00551-1_5.

(22) Andaleeb, H.; Ullah, N.; Falke, S.; Perbandt, M.; Brognaro, H.; Betzel, C. High-Resolution Crystal Structure and Biochemical Characterization of a GH11 Endoxylanase from Nectria Haematococca. *Sci. Rep.* **2020**, *10* (1), 15658. https://doi.org/10/gmptpq.

(23) Wiedorn, M. O.; Oberthur, D.; Bean, R.; Schubert, R.; Werner, N.; Abbey, B.; Aepfelbacher, M.; Adriano, L.; Allahgholi, A.; Al-Qudami, N.; Andreasson, J.; Aplin, S.; Awel, S.; Ayyer, K.; Bajt, S.; Barak, I.; Bari, S.; Bielecki, J.; Botha, S.; Boukhelef, D.; Brehm, W.; Brockhauser, S.; Cheviakov, I.; Coleman, M. A.; Cruz-Mazo, F.; Danilevski, C.; Darmanin, C.; Doak, R. B.; Domaracky, M.; Dorner, K.; Du, Y.; Fangohr, H.; Fleckenstein, H.; Frank, M.; Fromme, P.; Ganan-Calvo, A. M.; Gevorkov, Y.; Giewekemeyer, K.; Ginn, H. M.; Graafsma, H.; Graceffa, R.; Greiffenberg, D.; Gumprecht, L.; Gottlicher, P.; Hajdu, J.; Hauf, S.; Heymann, M.; Holmes, S.; Horke, D. A.; Hunter, M. S.; Imlau, S.; Kaukher, A.; Kim, Y.; Klyuev, A.; Knoska, J.; Kobe, B.; Kuhn, M.; Kupitz, C.; Kupper, J.; Lahey-Rudolph, J. M.; Laurus, T.; Le Cong, K.; Letrun, R.; Xavier, P. L.; Maia, L.; Maia, F.; Mariani, V.; Messerschmidt, M.; Metz, M.; Mezza, D.; Michelat, T.; Mills, G.; Monteiro, D. C. F.; Morgan, A.; Muhlig, K.; Munke, A.; Munnich, A.; Nette, J.; Nugent, K. A.; Nuguid, T.; Orville, A. M.; Pandey, S.; Pena, G.; Villanueva-Perez, P.; Poehlsen, J.; Previtali, G.; Redecke, L.; Riekehr, W. M.; Rohde, H.; Round, A.; Safenreiter, T.; Sarrou, I.; Sato, T.; Schmidt, M.; Schmitt, B.; Schonherr, R.; Schulz, J.; Sellberg, J. A.; Seibert, M. M.; Seuring, C.; others. Megahertz Serial Crystallography. *Nat Commun*, 2018, *9*, 4025. https://doi.org/10.1038/s41467-018-06156-7.

(24) Bui, S.; von Stetten, D.; Jambrina, P. G.; Prangé, T.; Colloc'h, N.; de Sanctis, D.; Royant, A.; Rosta, E.; Steiner, R. A. Direct Evidence for a Peroxide Intermediate and a Reactive Enzyme–Substrate–Dioxygen Configuration in a Cofactor-Free Oxidase. *Angew. Chem. Int. Ed.* **2014**, *53* (50), 13710–13714. https://doi.org/10.1002/anie.201405485.

(25) Stevenson, H. P.; Lin, G.; Barnes, C. O.; Sutkeviciute, I.; Krzysiak, T.; Weiss, S. C.; Reynolds, S.; Wu, Y.; Nagarajan, V.; Makhov, A. M.; Lawrence, R.; Lamm, E.; Clark, L.; Gardella, T. J.; Hogue, B. G.; Ogata, C. M.; Ahn, J.; Gronenborn, A. M.; Conway, J. F.; Vilardaga, J.-P.; Cohen, A. E.; Calero, G. Transmission Electron Microscopy for the Evaluation and Optimization of Crystal Growth. *Acta Crystallogr. Sect. Struct. Biol.* **2016**, *72* (5), 603–615. https://doi.org/10.1107/S2059798316001546.

(26) Mariani, V.; Morgan, A.; Yoon, C. H.; Lane, T. J.; White, T. A.; O'Grady, C.; Kuhn, M.; Aplin, S.; Koglin, J.; Barty, A.; Chapman, H. N. OnDA: Online Data Analysis and Feedback for Serial X-Ray Imaging. *J Appl Crystallogr*, 2016, *49*, 1073–1080. https://doi.org/10.1107/S1600576716007469.
(27) White, T. A.; Mariani, V.; Brehm, W.; Yefanov, O.; Barty, A.; Beyerlein, K. R.; Chervinskii, F.; Galli, L.; Gati, C.; Nakane, T.; Tolstikova, A.; Yamashita, K.; Yoon, C. H.; Diederichs, K.; Chapman, H. N. Recent Developments in CrystFEL. *J Appl Crystallogr*, 2016, *49*, 680–689. https://doi.org/10.1107/S1600576716004751.
(28) White, T. A.; Kirian, R. A.; Martin, A. V.; Aquila, A.; Nass, K.; Barty, A.; Chapman, H. N. CrystFEL: A Software Suite for Snapshot Serial Crystallography. *J. Appl. Crystallogr.* **2012**, *45* (2), 335–341. https://doi.org/10.1107/S0021889812002312.
(29) Gevorkov, Y.; Yefanov, O.; Barty, A.; White, T. A.; Mariani, V.; Brehm, W.; Tolstikova, A.; Grigat, R. R.; Chapman, H. N. XGANDALF - Extended Gradient Descent Algorithm for Lattice Finding. *Acta Crystallogr. Sect. Found. Adv.* **2019**, *75* (Pt 5), 694–704. https://doi.org/10.1107/S2053273319010593.
(30) Kabsch, W. XDS. *Acta Crystallographica Section D*, 2010, *66*, 125–132. https://doi.org/doi:10.1107/S0907444909047337.
(31) Battye, T. G. G.; Kontogiannis, L.; Johnson, O.; Powell, H. R.; Leslie, A. G. W. IMOSFLM: A New Graphical Interface for Diffraction-Image Processing with MOSFLM. *Acta Crystallographica Section D*, 2010, *67*, 271–281. https://doi.org/doi:10.1107/S0907444910048675.
(32) Duisenberg, A. J. M. Indexing in Single-Crystal Diffractometry with an Obstinate List of Reflections. *J. Appl. Crystallogr.* **1992**, *25* (2), 92–96. https://doi.org/10/fgpj8h.
(33) Brehm, W.; Diederichs, K. Breaking the Indexing Ambiguity in Serial Crystallography. *Acta Crystallogr D Biol Crystallogr*, 2014, *70*, 101–109. https://doi.org/10.1107/S1399004713025431.
(34) Winn, M. D.; Ballard, C. C.; Cowtan, K. D.; Dodson, E. J.; Emsley, P.; Evans, P. R.; Keegan, R. M.; Krissinel, E. B.; Leslie, A. G.; McCoy, A.; McNicholas, S. J.; Murshudov, G. N.; Pannu, N. S.; Potterton, E. A.; Powell, H. R.; Read, R. J.; Vagin, A.; Wilson, K. S. Overview of the CCP4 Suite and Current Developments. *Acta Crystallogr D Biol Crystallogr*, 2011, *67*, 235–242. https://doi.org/10.1107/S0907444910045749.
(35) Adams, P. D.; Afonine, P. V.; Bunkoczi, G.; Chen, V. B.; Davis, I. W.; Echols, N.; Headd, J. J.; Hung, L. W.; Kapral, G. J.; Grosse-Kunstleve, R. W.; McCoy, A. J.; Moriarty, N. W.; Oeffner, R.; Read, R. J.; Richardson, D. C.; Richardson, J. S.; Terwilliger, T. C.; Zwart, P. H. PHENIX: A Comprehensive Python-Based System for Macromolecular Structure Solution. *Acta Crystallogr D Biol Crystallogr*, 2010, *66*, 213–221. https://doi.org/10.1107/S0907444909052925.
(36) Afonine, P. V.; Grosse-Kunstleve, R. W.; Echols, N.; Headd, J. J.; Moriarty, N. W.; Mustyakimov, M.; Terwilliger, T. C.; Urzhumtsev, A.; Zwart, P. H.; Adams, P. D. Towards Automated Crystallographic Structure Refinement with Phenix.Refine. *Acta Crystallogr D Biol Crystallogr*, 2012, *68*, 352–367. https://doi.org/10.1107/S0907444912001308.
(37) Painter, J.; Merritt, E. A. TLSMD Web Server for the Generation of Multi-Group TLS Models. *J. Appl. Crystallogr.* **2006**, *39* (1), 109–111. https://doi.org/10/b4dbbk.
(38) Emsley, P.; Lohkamp, B.; Scott, W. G.; Cowtan, K. Features and Development of Coot. *Acta Crystallographica Section D*, 2010, *66*, 486–501. https://doi.org/doi:10.1107/S0907444910007493.

(39) Chen, V. B.; Arendall, 3rd, W. B.; Headd, J. J.; Keedy, D. A.; Immormino, R. M.; Kapral, G. J.; Murray, L. W.; Richardson, J. S.; Richardson, D. C. MolProbity: All-Atom Structure Validation for Macromolecular Crystallography. *Acta Crystallogr D Biol Crystallogr*, 2010, *66*, 12–21. https://doi.org/10.1107/S0907444909042073.

(40) Murshudov, G. N.; Skubak, P.; Lebedev, A. A.; Pannu, N. S.; Steiner, R. A.; Nicholls, R. A.; Winn, M. D.; Long, F.; Vagin, A. A. REFMAC5 for the Refinement of Macromolecular Crystal Structures. *Acta Crystallogr D Biol Crystallogr*, 2011, *67*, 355–367. https://doi.org/10.1107/S0907444911001314.

(41) Steiner, R. A.; Lebedev, A. A.; Murshudov, G. N. Fisher's Information in Maximum-Likelihood Macromolecular Crystallographic Refinement. *Acta Crystallogr. D Biol. Crystallogr.* **2003**, *59* (12), 2114–2124. https://doi.org/10.1107/S0907444903018675.

(42) Long, F.; Nicholls, R. A.; Emsley, P.; Gražulis, S.; Merkys, A.; Vaitkus, A.; Murshudov, G. N. AceDRG: A Stereochemical Description Generator for Ligands. *Acta Crystallogr. Sect. Struct. Biol.* **2017**, *73* (2), 112–122. https://doi.org/10.1107/S2059798317000067.

(43) Gražulis, S.; Daškevič, A.; Merkys, A.; Chateigner, D.; Lutterotti, L.; Quirós, M.; Serebryanaya, N. R.; Moeck, P.; Downs, R. T.; Le Bail, A. Crystallography Open Database (COD): An Open-Access Collection of Crystal Structures and Platform for World-Wide Collaboration. *Nucleic Acids Res.* **2012**, *40* (D1), D420–D427. https://doi.org/10.1093/nar/gkr900.

(44) Pettersen, E. F.; Goddard, T. D.; Huang, C. C.; Meng, E. C.; Couch, G. S.; Croll, T. I.; Morris, J. H.; Ferrin, T. E. UCSF ChimeraX: Structure Visualization for Researchers, Educators, and Developers. *Protein Sci. Publ. Protein Soc.* **2021**, *30* (1), 70–82. https://doi.org/10.1002/pro.3943.

(45) Juers, D. H.; Ruffin, J. MAP_CHANNELS: A Computation Tool to Aid in the Visualization and Characterization of Solvent Channels in Macromolecular Crystals. *J. Appl. Crystallogr.* **2014**, *47* (6), 2105–2108. https://doi.org/10.1107/S160057671402281X.

(46) Perbandt, M.; Werner, N.; Prester, A.; Rohde, H.; Aepfelbacher, M.; Hinrichs, W.; Betzel, C. Structural Basis to Repurpose Boron-Based Proteasome Inhibitors Bortezomib and Ixazomib as β-Lactamase Inhibitors. *Sci. Rep.* **2022**, *12* (1), 5510. https://doi.org/10.1038/s41598-022-09392-6.

(47) Nave, C.; Garman, E. F. Towards an Understanding of Radiation Damage in Cryocooled Macromolecular Crystals. *J. Synchrotron Radiat.* **2005**, *12* (3), 257–260. https://doi.org/10.1107/S0909049505007132.

(48) Southworth-Davies, R. J.; Medina, M. A.; Carmichael, I.; Garman, E. F. Observation of Decreased Radiation Damage at Higher Dose Rates in Room Temperature Protein Crystallography. *Structure* **2007**, *15* (12), 1531–1541. https://doi.org/10.1016/j.str.2007.10.013.

(49) Bui, S.; Steiner, R. A. New Insight into Cofactor-Free Oxygenation from Combined Experimental and Computational Approaches. *Curr. Opin. Struct. Biol.* **2016**, *41*, 109–118. https://doi.org/10.1016/j.sbi.2016.06.015.

(50) Zeldin, O. B.; Brockhauser, S.; Bremridge, J.; Holton, J. M.; Garman, E. F. Predicting the X-Ray Lifetime of Protein Crystals. *Proc. Natl. Acad. Sci.* **2013**, *110* (51), 20551–20556. https://doi.org/10.1073/pnas.1315879110.

(51) Bury, C. S.; Brooks-Bartlett, J. C.; Walsh, S. P.; Garman, E. F. Estimate Your Dose: RADDOSE-3D. *Protein Sci.* **2018**, *27* (1), 217–228. https://doi.org/10.1002/pro.3302.

(52) Mehrabi, P.; Stetten, D. von; Leimkohl, J.-P.; Tellkamp, F.; Schulz, E. C. An Environmental Control Box for Serial Crystallography Enables Multi-Dimensional

Experiments. bioRxiv November 8, 2021, p 2021.11.07.467596. https://doi.org/10.1101/2021.11.07.467596.
(53) de la Cruz, M. J.; Hattne, J.; Shi, D.; Seidler, P.; Rodriguez, J.; Reyes, F. E.; Sawaya, M. R.; Cascio, D.; Weiss, S. C.; Kim, S. K.; Hinck, C. S.; Hinck, A. P.; Calero, G.; Eisenberg, D.; Gonen, T. Atomic-Resolution Structures from Fragmented Protein Crystals with the CryoEM Method MicroED. *Nat. Methods* **2017**, *14* (4), 399–402. https://doi.org/10.1038/nmeth.4178.
(54) de la Mora, E.; Coquelle, N.; Bury, C. S.; Rosenthal, M.; Holton, J. M.; Carmichael, I.; Garman, E. F.; Burghammer, M.; Colletier, J.-P.; Weik, M. Radiation Damage and Dose Limits in Serial Synchrotron Crystallography at Cryo- and Room Temperatures. *Proc. Natl. Acad. Sci.* **2020**, *117* (8), 4142–4151. https://doi.org/10.1073/pnas.1821522117.
(55) Nass, K. Radiation Damage in Protein Crystallography at X-Ray Free-Electron Lasers. *Acta Crystallogr. Sect. Struct. Biol.* **2019**, *75* (2), 211–218. https://doi.org/10.1107/S2059798319000317.
(56) Weik, M.; Ravelli, R. B. G.; Kryger, G.; McSweeney, S.; Raves, M. L.; Harel, M.; Gros, P.; Silman, I.; Kroon, J.; Sussman, J. L. Specific Chemical and Structural Damage to Proteins Produced by Synchrotron Radiation. *Proc. Natl. Acad. Sci.* **2000**, *97* (2), 623–628. https://doi.org/10.1073/pnas.97.2.623.
(57) Burmeister, W. P. Structural Changes in a Cryo-Cooled Protein Crystal Owing to Radiation Damage. *Acta Crystallogr. D Biol. Crystallogr.* **2000**, *56* (3), 328–341. https://doi.org/10.1107/S0907444999016261.
(58) Ravelli, R. B.; McSweeney, S. M. The 'Fingerprint' That X-Rays Can Leave on Structures. *Structure* **2000**, *8* (3), 315–328. https://doi.org/10.1016/S0969-2126(00)00109-X.
(59) Yano, J.; Kern, J.; Irrgang, K.-D.; Latimer, M. J.; Bergmann, U.; Glatzel, P.; Pushkar, Y.; Biesiadka, J.; Loll, B.; Sauer, K.; Messinger, J.; Zouni, A.; Yachandra, V. K. X-Ray Damage to the Mn4Ca Complex in Single Crystals of Photosystem II: A Case Study for Metalloprotein Crystallography. *Proc. Natl. Acad. Sci.* **2005**, *102* (34), 12047–12052. https://doi.org/10.1073/pnas.0505207102.
(60) Ebrahim, A.; Appleby, M. V.; Axford, D.; Beale, J.; Moreno-Chicano, T.; Sherrell, D. A.; Strange, R. W.; Hough, M. A.; Owen, R. L. Resolving Polymorphs and Radiation-Driven Effects in Microcrystals Using Fixed-Target Serial Synchrotron Crystallography. *Acta Crystallogr. Sect. Struct. Biol.* **2019**, *75* (2), 151–159. https://doi.org/10.1107/S2059798318010240.
(61) Gotthard, G.; Aumonier, S.; De Sanctis, D.; Leonard, G.; von Stetten, D.; Royant, A. Specific Radiation Damage Is a Lesser Concern at Room Temperature. *IUCrJ* **2019**, *6* (4), 665–680. https://doi.org/10.1107/S205225251900616X.

	ALL	**10K (run13)**	**Ultrafast (run15_5K)**	**40K xylanase**	**4k Xylanase**	**10k Xylanase**	**1k Xylanase**	**UOX**
PDB								
Temperature (K)	293							
No. of collected images	127170	10382	5000	40000	4000	10000	1000	171340
Total measuring time (s)	5086	415.3	200	1600	160	400	40	6854
Average acquisition rate (frames s^{-1})	25							
Indexed lattices	61331	4286	5109	41508	4402	10807	1161	3142
Indexed per second	12.1	10.3	25.6	25.9	27.5	27.0	29.0	0.5
Space group	$P3_221$			C121				*I*222
a, b, c (Å)	42.16, 42.16, 234.35			80.55, 38.85, 53.57				79.79, 96.03, 105.21
α , β , γ (°)	90, 90, 120			90, 91, 90				90, 90, 90
Resolution (Å)	1.40-17.77 (1.40-1.42)	1.55-17.77 (1.55-1.58)	1.55-17.77 (1.55-1.58)	1.51-17.16 (1.51-1.54)	1.70-17.16 (1.70-1.73)	1.63-17.50 (1.63-1.66)	1.90—16.92 (1.90-1.93)	2.30-17.07 (2.30-2.34)
Unique reflections	49225	36504	36495	25916	18431	20896	13235	18265 (1796)
$\langle I/\sigma(I)\rangle$	9.11 (0.69)	3.25 (0.62)	3.75 (0.63)	5.83 (0.55)	2.64 (0.47)	3.67 (0.66)	1.91 (0.68)	2.44 (0.52)
Completeness (%)	100 (100)	99.98 (100)	99.98 (100)	98.75 (87.48)	100 (100)	100 (100)	99.73 (99.33)	99.98 (100)
Multiplicity	2217 (1400)	114 (65.0)	149 (75.1)	432 (43.8)	59 (28.1)	134 (53.5)	20.98 (13.2)	28.20 (20.6)
R_{split}	7.2 (165.91)	27.8 (172.41)	22.97 (170.30)	13.42 (248.68)	31.81 (245.34)	22.55 (168.38)	52.40 (169.81)	36.68 (193.69)
$CC_{1/2}$	0.991 (0.266)	0.815 (0.268)	0.907 (0.262)	0.987 (0.152)	0.910 (0.158)	0.960 (0.189)	0.751 (0.185)	0.849 (0.225)
CC*	0.998 (0.648)	0.948 (0.650)	0.975 (0.644)	0.997 (0.514)	0.976 (0.522)	0.990 (0.564)	0.926 (0.559)	0.958 (0.606)
Wilson *B* factor (Å²)	24.22 A^2	24.31 A^2	23.43 A^2	21.76	23.23	22.95	18.68	27.31
Resolution range	1.40-17.78 (1.40-1.47)	1.55-16.54 (1.55-1.67)	1.55-14.98 (1.55-1.67)	1.51 - 16.92 (1.51 - 1.57)	1.70 - 16.92 (1.7 - 1.761)	1.63 - 16.92 (1.63 - 1.69)	1.90 – 16.92 (1.90-2.00)	2.30 – 17.08 (2.30-2.36)
Reflections used in refinement	49225 (4832)	36504 (3545)	36495 (3544)	25571 (2028)	18305 (1704)	20858 (2067)	13227 (1286)	17361 (1274)
Reflections used for R-free	1033 (100)	768 (74)	765 (73)	1985 (156)	1415 (128)	1618 (159)	1021 (95)	919 (60)
R-work	0.1410 (0.3338)	0.1796 (0.2807)	0.1803 (0.3572)	0.1516 (0.3561)	0.1890 (0.3535)	0.1625 (0.3257)	0.2272 (0.3083)	0.2182 (0.366)
R-free	0.1561 (0.3827)	0.2116 (0.3130)	0.2023 (0.3405)	0.1831 (0.3590)	0.2203 (0.3787)	0.2104 (0.3683)	0.2617 (0.3571)	0.2661 (0.348)
RMS(bonds)	0.009	0.005	0.011	0.009	0.008	0.010	0.004	0.008
RMS(angles)	1.01	0.76	1.12	1.06	0.72	1.07	0.626	1.388
Ramachandran favored (%)	97.68	97.69	98.07	96.26	96.26	96.26	95.72	96.92
Ramachandran allowed (%)	1.93	1.92	1.54	3.21	3.74	3.74	4.28	3.08
Ramachandran outliers (%)	0.39	0.38	0.39	0.53	0.00	0.00	0.00	0.00
Rotamer outliers (%)	1.87	0.90	0.94	2.86	2.92	2.86	2.34	0.00
Clashscore	2.19	4.94	2.49	5.17	3.61	5.17	9.24	0.62
Average B-factor	34.26	32.76	34.43	23.58	24.78	23.57	23.74	39.13
macromolecules	33.23	31.48	32.70	21.32	22.53	21.23	22.44	39.40
solvent	45.06	46.83	46.80	39.88	37.22	39.55	32.03	34.69
ligands	78.08	44.91	90.63					33.48
MolProbity Score	1.27	1.27	0.89	1.85	1.79	1.83	2.07	

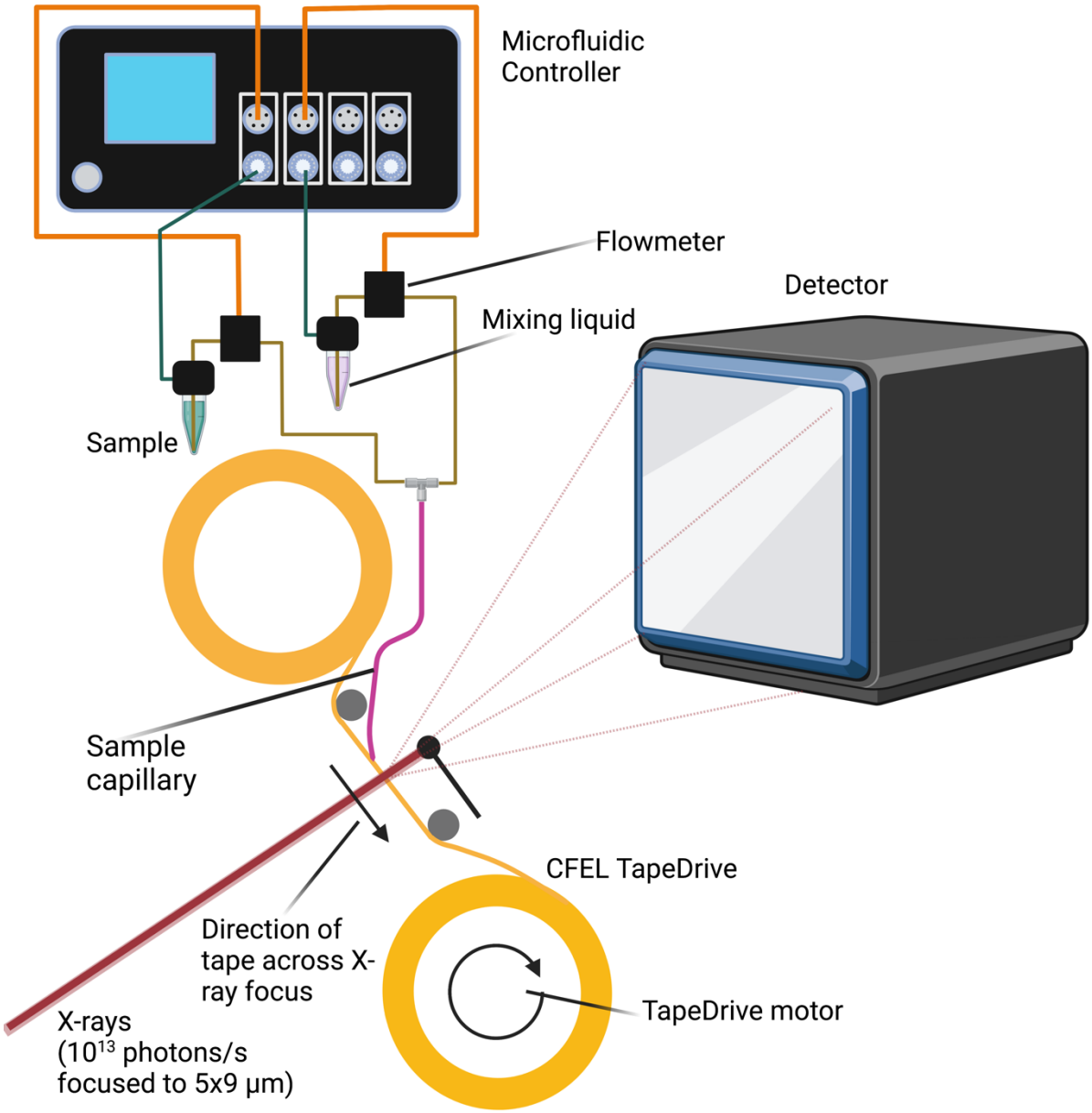

Figure 1 Schematic of the TapeDrive set-up as used in this study. The sample capillary can be used with and without mixing, the installation remains the same. The microfluidic controller is connected to the approx. 6 bar pressurized air available at PETRAIII. The microfluidic controller and TapeDrive are controlled through a notebook that can be operated remotely from the hutch. The TapeDrive is mounted on the motors that otherwise move the goniometer.

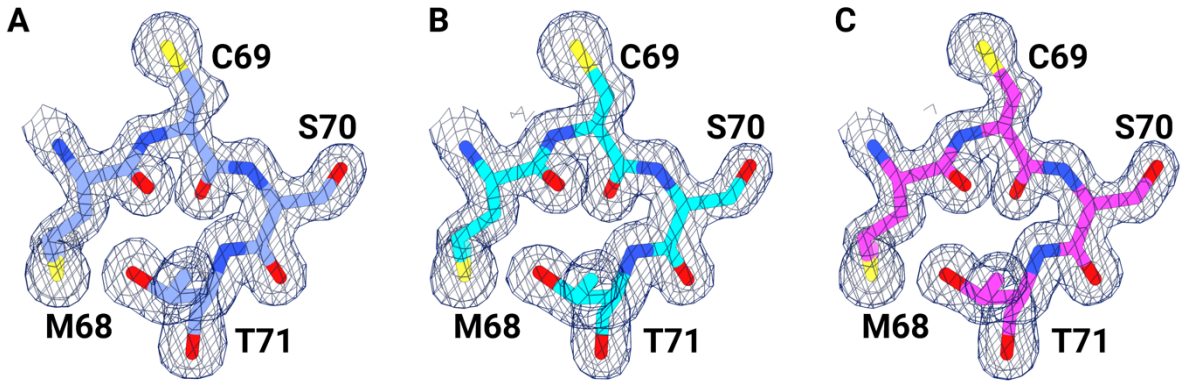

Figure 2 selected residues of CTX-M-14 β-lactamase around the active center and overlayed with the corresponding 2mFo-Fc maps contoured each at 1.5 sigma. A) 10'000 detector images (10K) B) 5'000 detector images (5K) C) full dataset (127'171 detector images). For A) and B) data out to 1.55 A was used, for C) the CC statistics indicated that data out to 1.4 A could be used. No significant differences between the electron density maps are visible.*

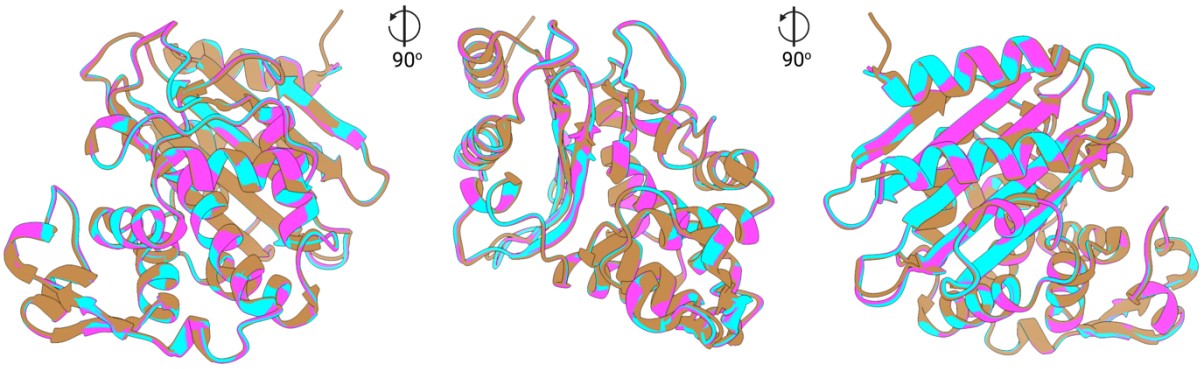

Figure 3 Comparison of the overall structures of CTX-M-14 β-lactamase from this study (cyan: 5K dataset; magenta: full dataset) and the cryoMX structure (PDB accession code: 7q0z, brown). It can be seen, that besides the differences in symmetry and unit cell dimensions, the asymmetric units align very well.

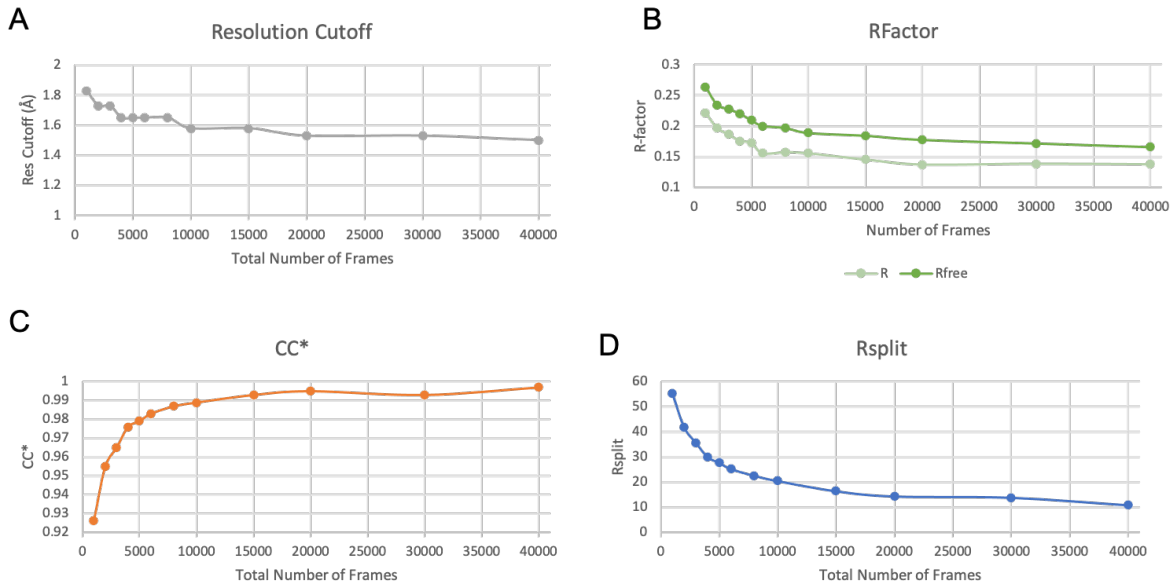

Figure 4A) evolution of resolution cut-off (resolution at which CC is >0.5) as a function of addition of further detector frames. B) Evolution Rwork and Rfree values using the same starting model and refinement parameters and high resolution cut-off of 1.9A. C) overall CC* and D) overall Rsplit values as a function of detector frames added, calculated to a high resolution cut-off of 1.8A.*

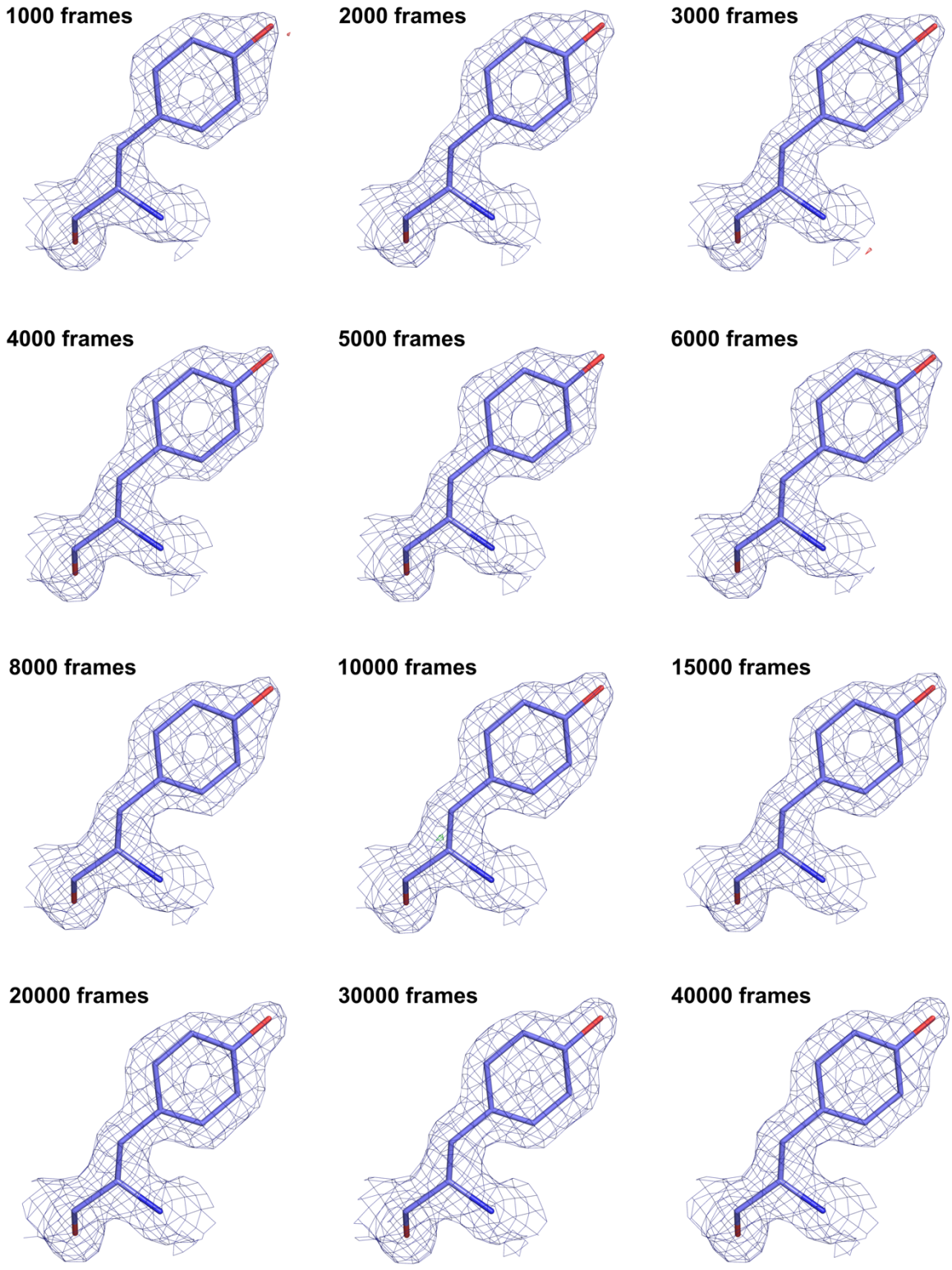

Figure 5 shows the sigma-weighted 2Fo-Fc electron density around Tyr41 of NhGH11 Xylanase for models refined against the datasets made using the stated number of frames. Resolution cut-off for all data-sets was 1.9 A and all maps are displayed at 1 sigma.

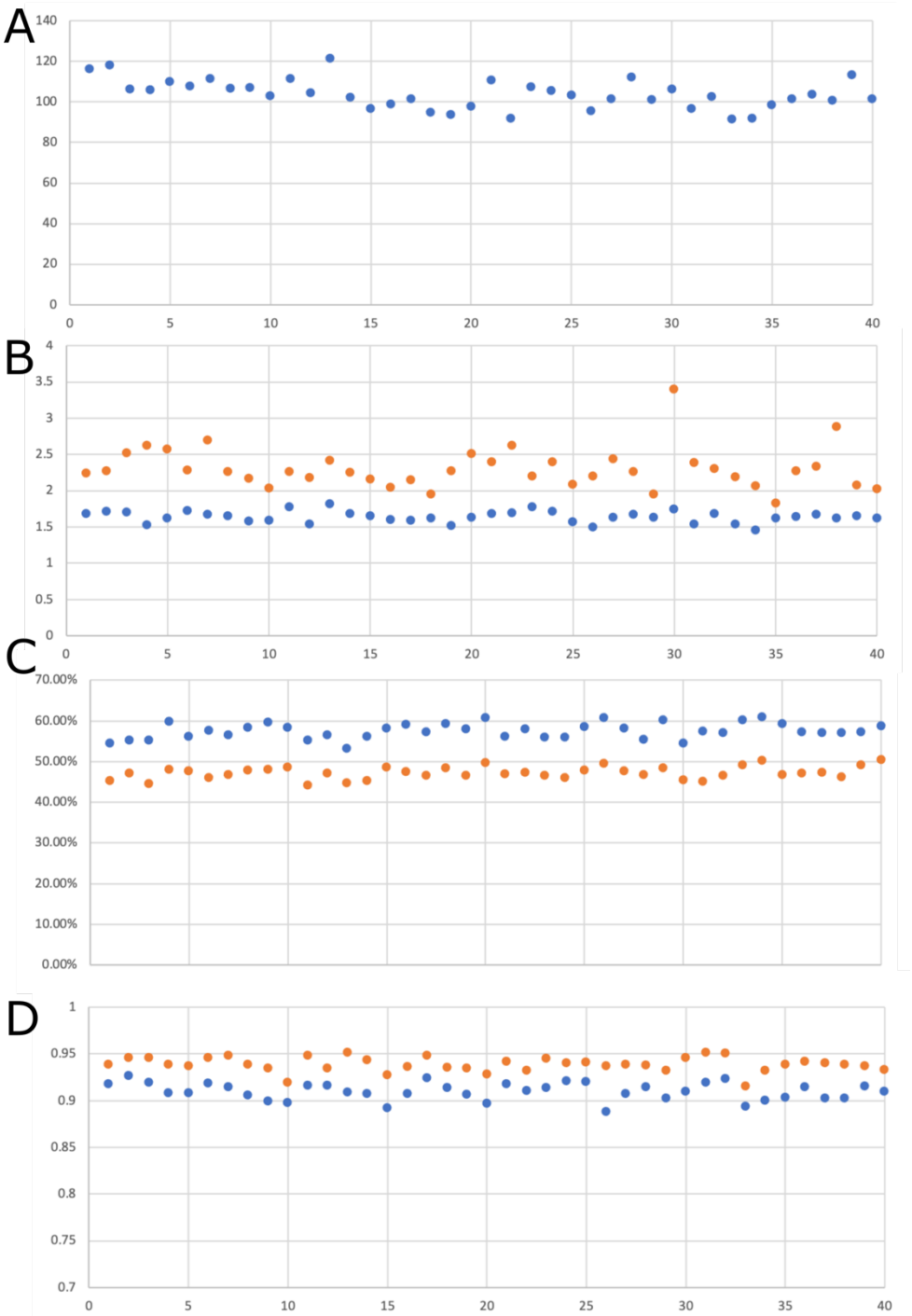

Figure 6 A) Indexing rate, B) SNR-, C) CC- and D) Rsplit-values for all 40 datasets, each consisting of 1000 recorded detector-frames within one run. In B), C) and D): values from processing without partiality modelling are depicted in blue, values from processing with partiality modelling are shown in orange.*

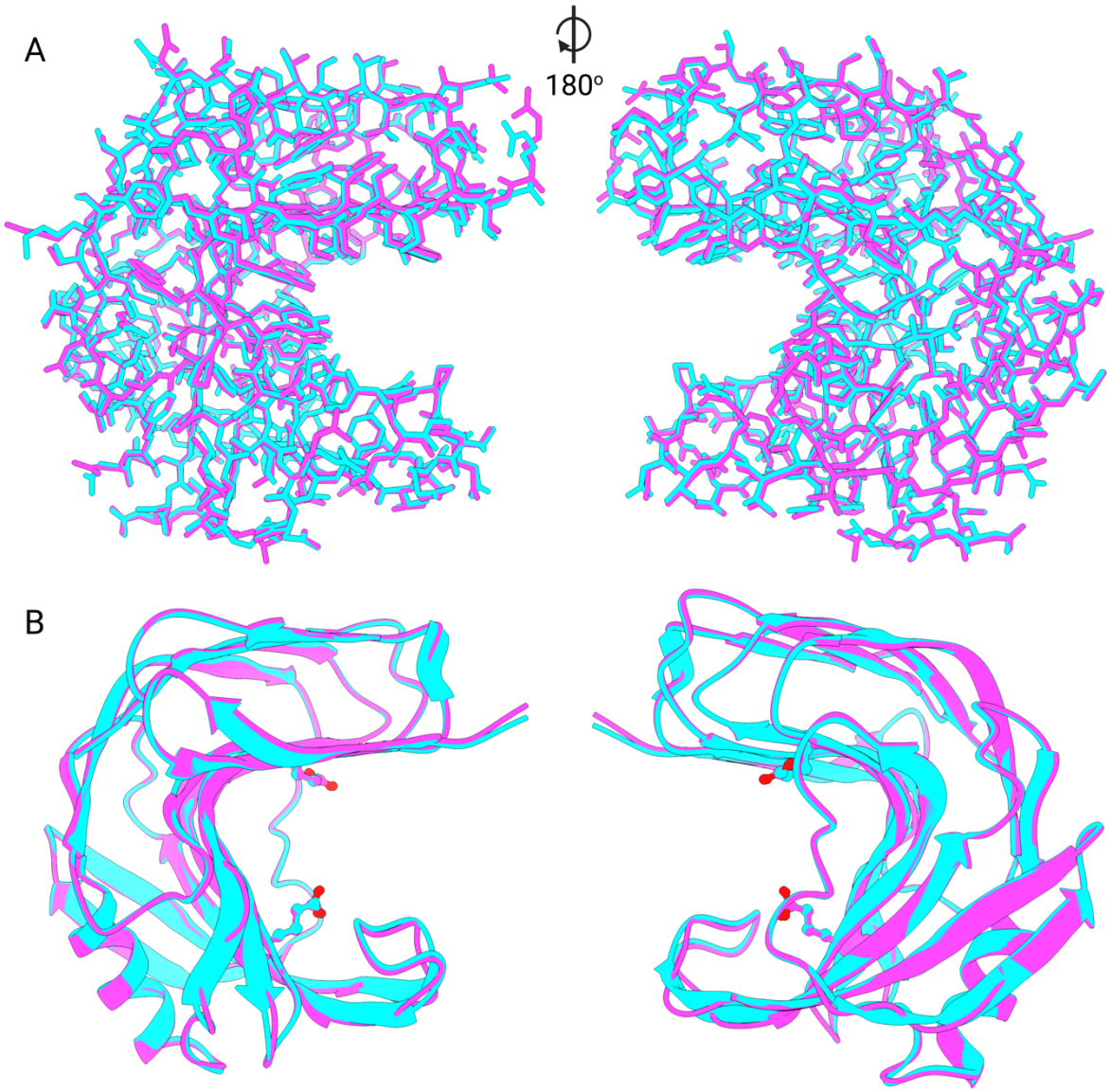

Figure 7 Comparison of the overall structures of NhGH11 xylanase obtained by cryoMX (cyan) and RT-SSX (magenta, 40'000 detector images dataset). A) shows the all atom "stick" depiction of the proteins, allowing to assess the alignment of the sidechains, B) shows the cartoon-plot for better visibility of the overall fold and additionally residues E89 and E180 that form the catalytic center. These residues overlap almost perfectly for both datasets.

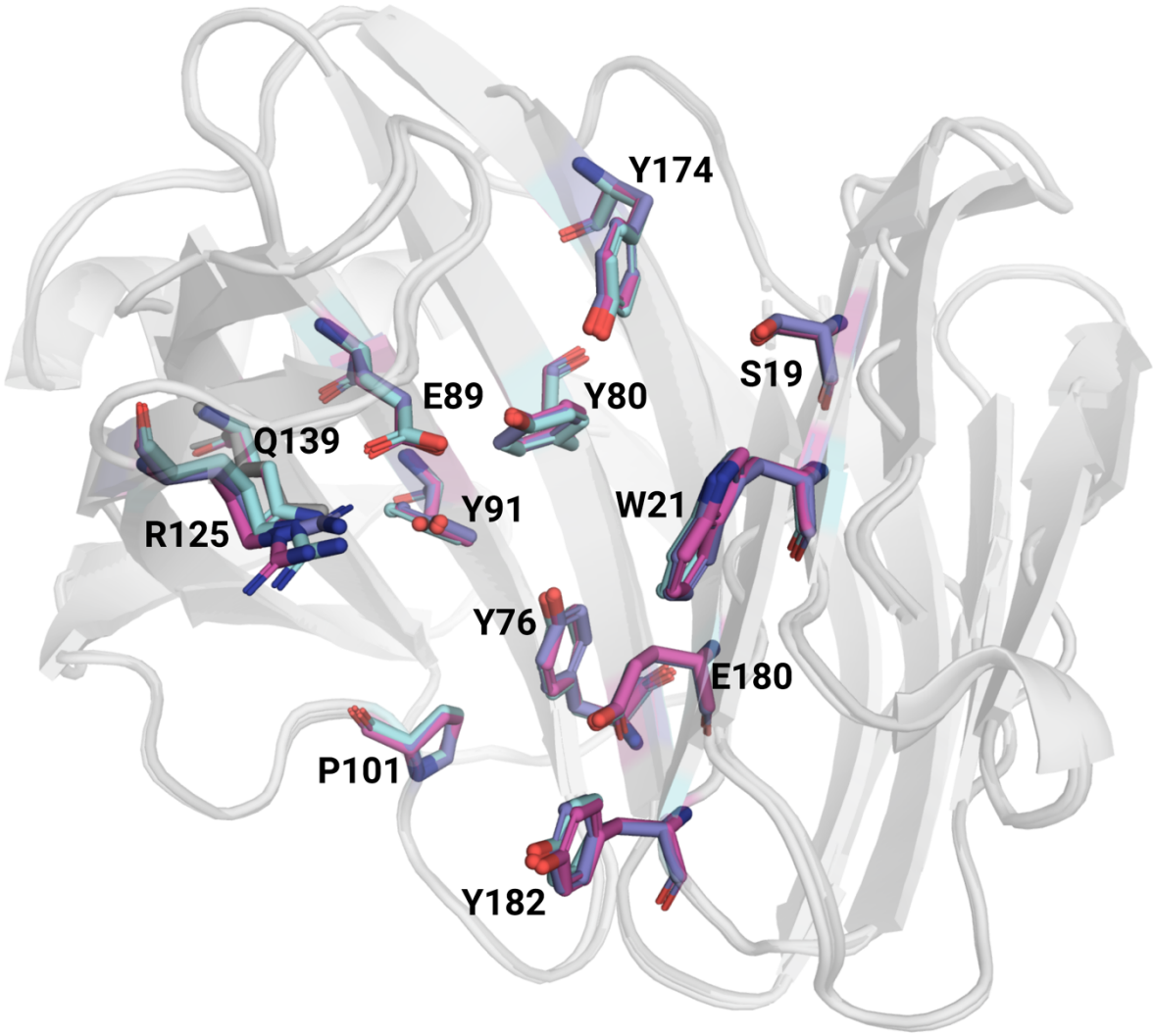

Figure 8 Detailed view of the alignment of all residues that compose the active site of NhGH11 xylanase. The cryoMX residues are shown in cyan, the full 40'000 detector images dataset structure in magenta and additionally the active site residues from the structure obtained by refinement against the 1000 detector images dataset are shown in purple. The strongest deviations from the cryoMX reference can be seen in Arg125, all other residues overlap almost perfectly.

Supplementary Information

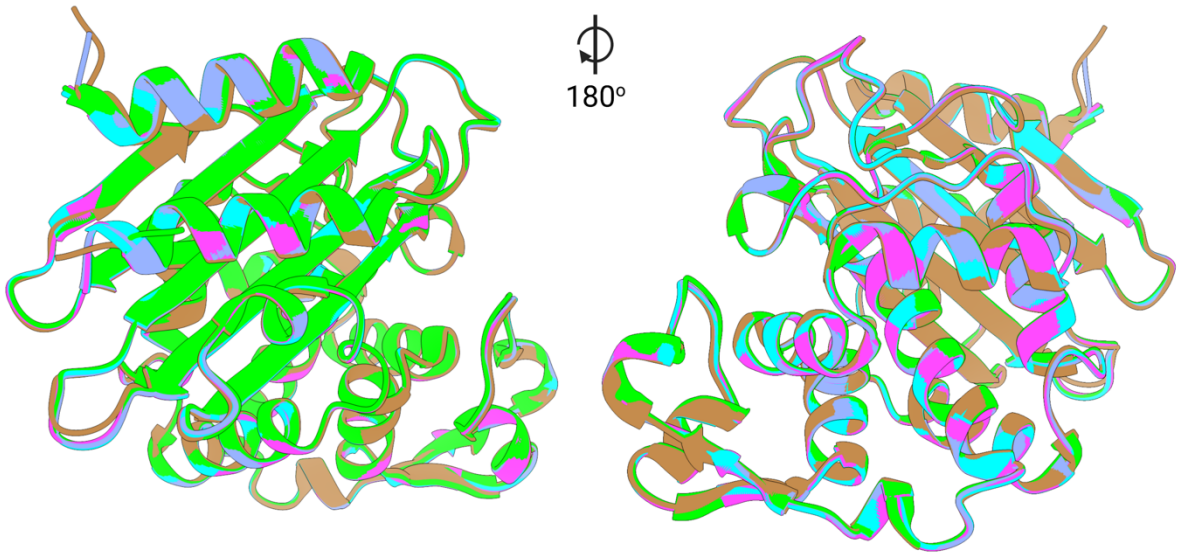

Figure S1 Aligned CTX-M-14 β-lactamase structures, cyan: 5K dataset; purple: 10K dataset; magenta: full dataset, brown: the cryoMX structure (PDB accession code: 7q0z) and green: the structure from EuXFEL (PDB accession code: 6GTH)

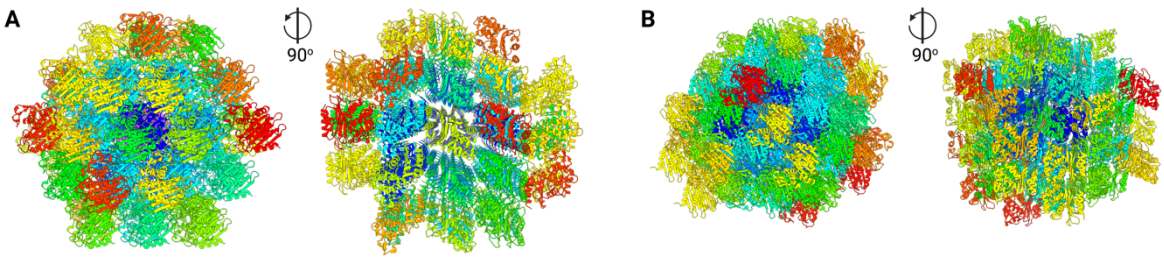

Figure S2: crystal packing of CTX-M-14 β-lactamase. A) from RT-SSX and B) from cryoMX (PDB accession code: 7q0z)

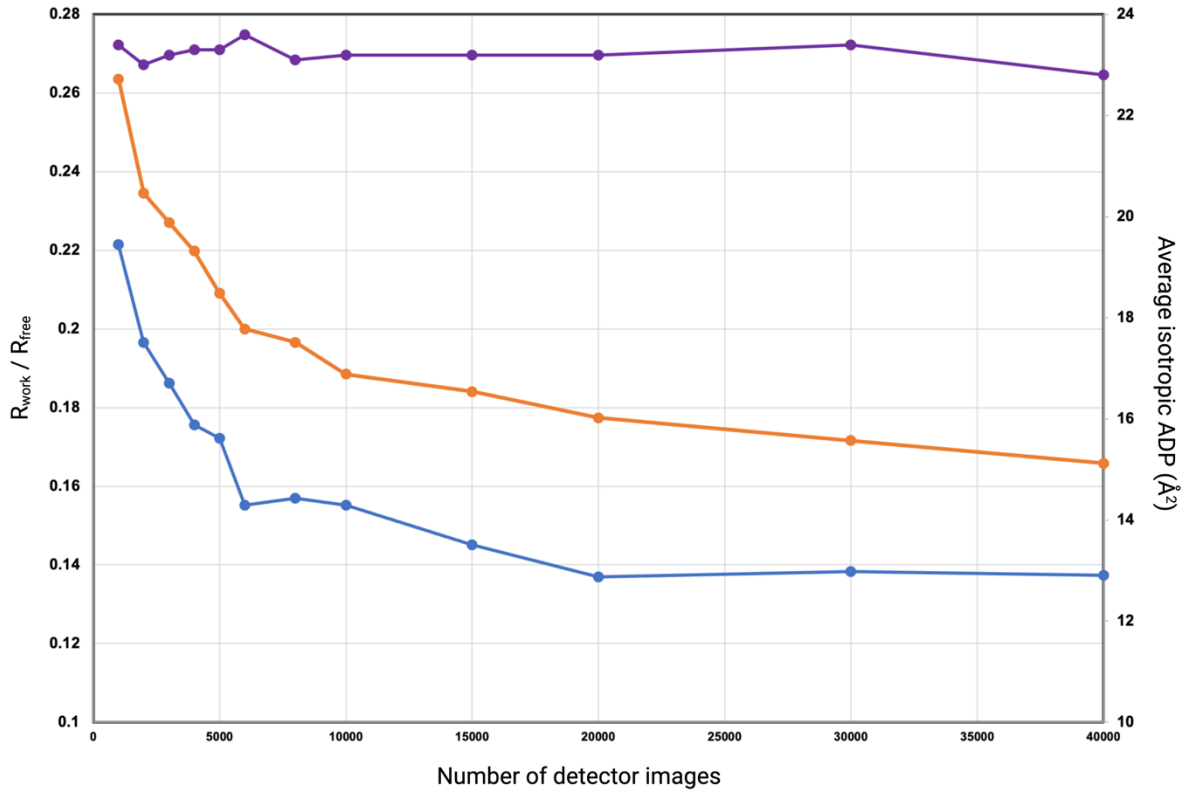

Figure S3 Plot of the evolution of Rfree (orange) Rwork (blue) and the average isotropic ADP (purple) with addition of detector images in automatic refinement of NhGH11 xylanase.

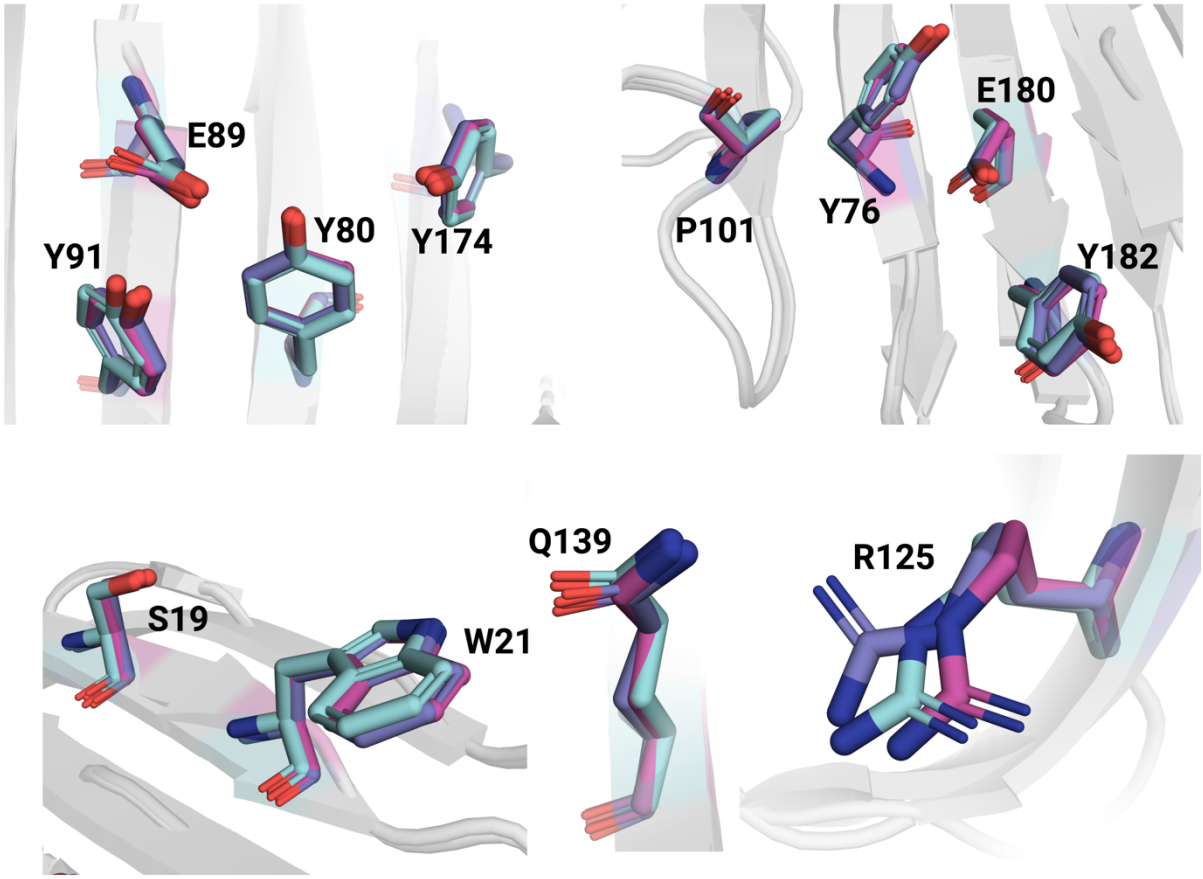

Figure S4 detailed comparison of the spatial positions of the active site residues of NhGH11 xylanase. The full (40'000 detector images) dataset residues are shown in magenta, the 1000 detector images dataset residues in purple and the cryoMX residues (PDB accession code: 6y0h) are shown in cyan.